A STUDY OF NICKEL INFLUENCE ON THE PROMOTION OF AUSFERRITE FORMATION IN Fe-Mo-Mn-Si-C-(Ni) SINTERED COMPOSITES

ZAYAR MIN HTIKE

A THESIS REPORT SUBMITTED IN PARTIAL FULFILLMENT
OF THE REQUIREMENTS FOR THE DEGREE OF
MASTER OF ENGINEERING IN AUTOMOTIVE AND ADVANCED TRANSPORTATION
ENGINEERING
SCHOOL OF ENGINEERING
KING MONGKUT'S INSTITUTE OF TECHNOLOGY LADKRABANG
YEAR 2024
KMITL-2024-EN-M-277-185

THESIS TITLE	A study of nickel influence on the promotion of ausferrite formation in Fe-Mo-Mn-Si-C-Ni sintered composites
STUDENT	Mr. Zayar Min Htike
STUDENT ID	64601185
DEGREE	Master of Engineering
PROGRAM	Automotive and Advanced Transportation Engineering
Year	2024
THESIS ADVISOR	Asst. Prof. Dr. Jittraporn Wongsa-ngam
CO-THESIS ADVISOR	Dr. Ruangdaj Tongsri

ABSTRACT

It is generally accepted that austempered ductile irons have mechanical properties promising for engineering applications. Recently, it has been found that it is possible to introduce austempered ductile iron microstructure to a sintered composite. Such introduction will not only improve sintered composite performance but also expand the applications of sintered materials. It was reported previously that sintered Fe-Mo-Mn-Si-C composite, produced from powder mixture of pre-alloyed Fe-1.50Mo-0.15Mn and 4.0 wt.% silicon carbide, showed microstructural feature consisting of black particles enveloped with ferrite halos, pearlite and ausferrite. In this work, it was hypothesized that the addition of austenite stabilizing elements would promote ausferrite fraction in sintered Fe-Mo-Mn-Si-C composite. Nickel was selected for this experimental work. It was found that nickel addition resulted in the replacement of pearlite by ausferrite. The sintered composite added with 1.0 wt.% nickel showed dual phase austempered ductile iron microstructure, i.e., the microstructural feature consisting of black particles enveloped with ferrite halos and ausferrite. The sintered composite added with 2.0 wt.% nickel showed austempered ductile iron microstructure, i.e., the microstructural feature consisting of black particles enveloped with ausferrite. Tensile properties of sintered composites were controlled by microstructural components. Among all experimental specimens, the sintered composite added with 1.0 wt.% nickel showed optimum tensile properties.

Keywords: Sintering, sintered composite, ausferrite, austempered ductile iron microstructure, tensile property.

ACKNOWLEDGEMENTS

I would like to express my heartfelt gratitude to everyone who has supported and contributed to the completion of this thesis. Without their invaluable assistance, guidance, and encouragement, this research would not have been possible. First and foremost, I am deeply grateful to my supervisors, Asst. Prof. Dr. Jittraporn Wongsa-ngam and Dr. Ruangdaj Tongsri, for their unwavering support and invaluable guidance throughout the entire process. Their expertise, patience, and insightful feedback have been instrumental in shaping this thesis and refining my research skills. I am truly fortunate to have had the opportunity to work under their mentorship.

I would also like to extend my sincere appreciation to my co-advisors, Dr. Ruangdaj Tongsri from NSTDA, and Prof. Dr. Naohto Ohtake from School of Engineering, Tokyo Institute of Technology, for their valuable insights, constructive criticism, and suggestions that have greatly enhanced the quality of this research. Their expertise and thorough review of my work have significantly contributed to its overall improvement.

My sincere thanks go to the staff, NSTDA (MTEC) laboratory members, (Mr. Monnapas Morakotjinda, Mrs. Thanyaporn Yotkaew, Mr. Pongsak Wila, Mr.Rungtip Krataitong and Mrs. Nattaya Tosangthum) for providing an enriching academic environment and necessary resources to support my research. Their dedication to fostering an atmosphere of intellectual growth and learning has been immensely beneficial.

Lastly, I would like to acknowledge the support and encouragement of my fellow classmates and colleagues who have been a source of inspiration and motivation. Their intellectual discussions, shared experiences, and camaraderie have enriched my academic pursuits and made this journey more meaningful.

Zayar Min Htike

TABLE OF CONTENTS

ABSTRACT I

ACKNOWLEDGEMENTS II

TABLE OF CONTENTS III

LIST OF TABLES VIII

LIST OF FIGURES IX

CHAPTER 1 1

INTRODUCTION 1

1.1 Research Background 1

1.2 Objectives 2

1.3 Scope of the Work 2

1.4 Expected Benefits 3

CHAPTER 2 4

Literature Review 4

2.1 Powder metallurgy (PM) 4

2.1.1 Powder characteristics 5

2.1.2 Powder Mixing 5

2.1.3 Powder Compaction 6

2.1.4 Sintering 7

2.1.5 Sintering Temperature 8

2.2 Alloying Element 9

2.2.1 Iron alloy phase diagram 9

2.2.2 Effect of alloying element on the formation of alloy carbides (Secondary hardening) 10

2.2.3 Effect on ferrite hardness 11

2.3 Self-lubricant material 12

2.3.1 Graphite 12

2.4 Microstructure 13
2.4.1 Ferrite 14
2.4.2 Pearlite 15
2.4.3 Ausferrite 15
2.5 Ductile cast iron or nodular cast iron 16
2.5.1 Austempered Ductile Iron 17
2.5.2 Fe-Mo-Si-C sintered composite with austempered ductile iron microstructure 17
2.5.3 Fe-Mo-Si-C composite with varied Mo content 18
2.6 Green Density 19
2.7 Tribological Test 20
2.7.1 The pin on disc wear tester 20
2.7.2 The friction coefficient 21
2.7.3 Wear rate 22
2.7.4 Mass loss 22
2.7.5 Volume loss 22
2.8 Wear mechanism 23
2.8.1 Adhesive wear 23
2.8.2 Abrasive wear 23
2.8.3 Fatigue/ Delamination wear 24
2.8.4 Corrosive/ Oxidative wear 25
CHAPTER 3 27
RESEARCH METHODOLOGY 27
3.1 Materials 27
3.1.1 Pre-alloyed Fe-Mo-Mn powder 27
3.1.2 Silicon carbide 27
3.1.3 Zinc stearate 28

3.1.4 Argon gas 28

3.1.5 Nital etchant..28

3.2 Experimental Equipment 29

3.2.1 Digital balance 29

3.2.2 Analytical balance 29

3.2.3 Powder blender..30

3.2.4 Hydraulic pressing machine..30

3.2.5 High vacuum sintering furnace 30

3.2.6 High precision cutting machine..31

3.2.7 Hot mounting press 31

3.2.8 Metallurgical Grinding Polishing Machine 32

3.2.9 Silicon Carbide paper 32

3.2.10 Polishing cloth..32

3.2.11 Diamond suspension 33

3.3 Characterization instruments 33

3.3.1 Digital vernier 33

3.3.2 Macro hardness testing machine..33

3.3.3 Universal testing machine (Instron 8801)..34

3.3.4 Optical Microscope..34

3.3.5 Scanning Electron Microscope 35

3.3.6 X-Ray Diffraction Analysis..35

3.3.7 Pin-on-disc testing machine 36

3.4 Experimental procedure 36

3.4.1 Mixing powder..36

3.4.2 Compaction 37

3.4.3 Sintering..38

3.5 Mechanical test ... 38
3.5.1 Hardness test ... 38
3.5.2 Tensile test ... 38
3.5.3 Surface preparation ... 39
3.6 Wear test ... 39
3.6.1 Microstructure Analysis ... 40
3.6.2 X-Ray Diffraction Analysis ... 40
CHAPTER 4 ... 41
RESULTS AND DISCUSSION ... 41
4.1 Microstructure ... 41
4.1.1 General microstructure characterization by using OM and SEM ... 41
4.1.2 Sintered 00Ni composite ... 45
4.1.3 Sintered 05Ni composite ... 46
4.1.4 Sintered 10Ni composite ... 48
4.1.5 Sintered 15Ni composite ... 49
4.1.6 Sintered 20Ni composite ... 51
4.2 The influence of Ni on black particles and ferrite halos ... 52
4.2.1 The influence of Ni on ausferrite fraction and component thickness ... 55
4.3 Mechanical properties ... 55
4.4 Friction coefficient ... 57
4.5 Wear rates ... 59
4.6 Worn surfaces and wear debris ... 60
4.6.1 Worn surfaces of all sintered composite at normal load 15N ... 60
4.6.2 Worn debris of all sintered composite at normal load 15N ... 62
4.6.3 Worn surfaces and wear debris of sintered 05Ni composite ... 62
4.6.4 Worn surfaces and wear debris of sintered 10Ni composite ... 65

4.6.5 Worn surfaces and wear debris of sintered 15Ni composite 67

4.6.6 Worn surfaces and wear debris of sintered 20Ni composite 69

4.6.7 A comparative discussion of current research to other’s research works 71

CHAPTER 5 73

CONCLUSIONS...73

References...74

APPENDIX A: 81

CONFERENCE PARTICIPATION 81

AUTHOR BIOGRAPHY..81

LIST OF TABLES

Table 3-1 The chemical composition of mixed powder 37
Table 4-1 Total area of each phase of sintered materials...42
Table 4-2 Coefficient of friction of all sintered composites with varied Nickel content 59
Table 4-3 Wear rate of Fe-Mo-Mn-Si-C-(Ni) sintered alloys under different Nickel content...60
Table 4-4 Comparison of current research to other’s research works............................71

LIST OF FIGURES

Figure 2-1 High strength sintered parts [10] 4
Figure 2-2 General P/M Processes [8] 5
Figure 2-3 V-type and double cone mixers [8] 6
Figure 2-4 Single and double acting powder compaction [8] 7
Figure 2-5 Schematic diagram of sintering process [11] 8
Figure 2-6 Sintered density time curves illustrating effects of increasing green density and sintering temperature on densification 8
Figure 2-7 Iron alloy phase diagrams: (a) open γ –field; (b) expanded γ – field; (c) closed γ –field; (d) contracted γ –field [12] 10
Figure 2-8 The influence of Mo on the tempering of quenched 0.1wt% C steels 11
Figure 2-9 Influence of alloying element on ferrite hardness 12
Figure 2-10 (a) flake graphite in grey cast iron [13], (b) graphite nodules in ductile cast iron [14] 13
Figure 2-11 Hardness of various microstructure of steels containing up to1.2wt.% C [15] 14
Figure 2-12 The optical micrograph of ferrite microstructure in low carbon steel 15
Figure 2-13 SEM micrographs of (a) fine pearlite (b)coarse pearlite in eutectoid steel [17] 15
Figure 2-14 OM image of ausferrite containing bainitic ferrite and austenite [18] 16
Figure 2-15 Bulls-eye structure of ductile cast iron or nodular cast iron [19] 17
Figure 2-16 SEM micrograph of ductile iron at different austempering temperatures [20] 17
Figure 2-17 Microstructure of Fe-Mo-SiC alloys (a) 0.85Mo (b) 1.50Mo 18
Figure 2-18 SEM micrographs of sintered composites (a) 0.00Mo, (b) 0.50Mo, (c) 0.85Mo, and (d) 1.50Mo [22] 19
Figure 2-19 The particles bonding at difference temperature. 20
Figure 2-20 The schematic of pin on disc wear tester. 21
Figure 2-21 The typical curve of friction coefficient and time 22
Figure 2-22 Schematic of adhesive wear mechanism 23
Figure 2-23 Schematic illustration of (a) two body abrasive wear mechanism and (b) three body abrasive wear mechanism 24

Figure 2-24 SEM micrograph of severe delamination wear. 25
Figure 2-25 SEM micrograph of mild delamination wear. 25
Figure 2-26 Schematic of oxidative wear mechanism. 26
Figure 2-27 SEM micrograph of oxidative wear. 26
Figure 3-1 Iron based particle powder. 27
Figure 3-2 SiC powder 27
Figure 3-3 Zinc stearate powder 28
Figure 3-4 Argon gas cylinders. 28
Figure 3-5 Nital etchant 29
Figure 3-6 The Digital balance (3-digit) 29
Figure 3-7 The Analytical balance (4-digit) 29
Figure 3-8 Powder blender 30
Figure 3-9 Hydraulic pressing machine 30
Figure 3-10 High vacuum sintering furnace SCHMETZ D59708 MENDEN 31
Figure 3-11 High precision cutting machine 31
Figure 3-12 Hot mounting press 31
Figure 3-13 Metallurgical Grinding Polishing Machine 32
Figure 3-14 Silicon Carbide paper 32
Figure 3-15 Micron polishing cloth 33
Figure 3-16 Diamond suspension size 6, 3 and 1 µm 33
Figure 3-17 Digital vernier 33
Figure 3-18 Instron-930 Macro hardness testing machine 34
Figure 3-19 Instron 8801 Universal Instrument 34
Figure 3-20 Optical microscope by Olympus STM7, Japan 35
Figure 3-21 Scanning electron microscope by Hitachi SU8230, Japan 35
Figure 3-22 X-Ray Diffraction Analysis 36
Figure 3-23 Pin-on-disc testing machine (ASTM G99) 36
Figure 3-24 The standard tensile test bars (MPIF standard 10, ASTM B783) 37
Figure 3-25 Dimensions of disk specimen 37
Figure 3-26 The sintering profile. 38
Figure 3-27 The schematic of ball-on-disc wear test set up 40
Figure 4-1 Optical micrographs of Fe-Mo-Mn-Si-C-Ni sintered composite 43
Figure 4-2 SEM micrographs of Fe-Mo-Mn-Si-C-Ni sintered composites 44

Figure 4-3 Investigation on microstructure of 00Ni sintered composite; (a) Optical micrograph image showing basic microstructural features, (b) Color OM image showing pearlite and upper ausferrite, (c) SEM image showing general microstructural features (d) SEM image showing bainitic ferrite, austenite, and upper ausferrite, and (e) XRD patterns of microstructural components..46

Figure 4-4 Investigation on microstructure of 05Ni sintered composite; (a) Optical micrograph image showing basic microstructural features, (b) Color optical micrograph image showing pearlite and upper ausferrite, (c) SEM image showing general microstructural features (d) SEM image showing bainitic ferrite, austenite and upper ausferrite, and (e) XRD patterns of microstructural components. 47

Figure 4-5 Investigation on microstructure of 10Ni sintered composite; (a) Optical micrograph image showing basic microstructural features, (b) Color OM image showing pearlite and upper ausferrite, (c) SEM image showing general microstructural features (d) SEM image showing bainitic ferrite, austenite, and upper ausferrite, and (e) XRD patterns of microstructural components..49

Figure 4-6 Investigation on microstructure of 15Ni sintered composite; (a) Optical micrograph image showing basic microstructural features, (b) Color OM image showing pearlite and ausferrite, (c) SEM image showing general microstructural features (d) SEM image showing bainitic ferrite, austenite, and lower ausferrite, and (e) XRD patterns of microstructural components..50

Figure 4-7 Investigation on microstructure of 20Ni sintered composite; (a) Optical micrograph image showing basic microstructural features, (b) Color OM image showing pearlite and ausferrite, (c) SEM image showing general microstructural features (d) SEM image showing bainitic ferrite, austenite, and lower ausferrite, and (e) XRD patterns of microstructural components..52

Figure 4-8 Electron probe microanalysis of sintered composites (a) SEM image of 20Ni, (b) C, (c) Si, (d) Ni, (e) Mn, (f) Mo, and (g) Fe. 54

Figure 4-9 Mechanical characteristics of Fe-Mo-Mn-Si-C-(Ni) sintered composites; (a) Ultimate tensile strength, (b) Yield strength, (c) Elongation, and (d) Macro-hardness. 56
Figure 4-10 The friction coefficient at load 5N of all sintered composites 58
Figure 4-11 The friction coefficient at load 10N of all sintered composites 58
Figure 4-12 The friction coefficient at load 15N of all sintered composites 58
Figure 4-13 Wear rate at load 5N, 10N and 15N of Fe-Mo-Mn-Si-C-(Ni) sintered composites. 60
Figure 4-14 SEM micrograph of worn surface of all sintered composites at load 15N 61
Figure 4-15 SEM micrograph of wear debris of all sintered composites at load 62
Figure 4-16 The SEM micrograph of the worn surface of sintered 05Ni composites....63
Figure 4-17 The SEM micrograph of wear debris of sintered 05Ni composite......64
Figure 4-18 The SEM micrograph of the worn surface of sintered 10Ni composites....65
Figure 4-19 The SEM micrograph of wear debris of sintered 10Ni composite......66
Figure 4-20 The SEM micrograph of the worn surface of sintered 15Ni composites....67
Figure 4-21 The SEM micrograph of wear debris of sintered 15Ni composite......68
Figure 4-22 The SEM micrograph of the worn surface of sintered 20Ni composites....69
Figure 4-23 The SEM micrograph of wear debris of sintered 20Ni composite......70

CHAPTER 1

INTRODUCTION

1.1 Research Background

In recent years, powder metallurgy is particularly attractive and advanced because it is a cost saving process to produce particulate-sintered composites which has higher mechanical strength and better wear resistance than the conventional castings/forgings. High strength sintered alloys are achieved through varied alloy composition, fine powder materials, binders/lubricants, and specific temperature control. PM materials dominated the automotive industry mostly while other applications are also increasingly popular [1]. Powder metallurgy has the benefit of combining sintering and heat treatment into a single step process known as sinter hardening which can produce unique microstructures to achieve desired mechanical properties by using metal composites and a controlled heat treatment. It can produce high-density, strong, and wear-resistant components, often in the form of sintered metal parts [2].

There has been a major interest in iron-based composites due to their ability to combine with ceramic particles to produce high strength and friction resistance sintered parts. A ferrite and pearlite cast iron produced by foundry has microstructure consisting of graphite nodule, ferrite, and pearlite. The decomposition of the austenite in the stable system forms ferrite halos growing symmetrically around graphite nodules. Pearlite appears as nodules inside the remaining austenite then forms at the ferrite/austenite matrix [3]. Surprisingly, ferrite-pearlite ductile iron microstructure was also observed in sintered composites, such as Fe-Mo-Si-C composites [4]. Later, sintered Fe-Mo-Si-C composites with varied Mo contents were explored for microstructures and mechanical properties. It was found that a special microstructural feature called ‘ausferrite’ consisting of ferrite and austenite coexisted with ferrite and pearlite in sintered Fe-Mo-Mn-Si-C composites with Mo contents of $\geqslant 0.85$ wt. % [5]. An austempered ductile iron with an ausferrite (bainitic ferritic + austenite) microstructure is commonly obtained by a heat treatment called ‘austempering’ of an as-cast ductile iron [6].

According to literature given above, the chemistry manipulation of sintered Fe-Mo-Si-C composites to have higher volume fraction of ausferrite is expected to be successful via nickel (Ni) addition. The reason behind this assumption is that Ni is a good austenite stabilizer, which is expected to synergize with Mo on ausferrite formation promotion [7]. In this research the influence of varied nickel contents in Fe-1.5Mo-0.15Mn pre-alloyed powders with 4wt.%SiC is studied on the microstructure, mechanical properties and tribological properties.

1.2 Objectives

This research aimed to achieve the following objectives.

- To produce sintered Fe-Mo-Mn-Si-C-Ni composite with varied nickel content and sintered Fe-Mo-Mn-Si-C as a referenced material.
- To investigate the formation mechanisms and differences among sintered Fe-Mo-Mn-Si-C-Ni composites and Fe-Mo-Mn-Si-C composite.
- To investigate the effects of Nickel on the microstructure and mechanical properties of sintered Fe-Mo-Mn-Si-C-Ni composites.
- To investigate the effects of Nickel on tribological properties and wear behaviour of sintered Fe-Mo-Mn-Si-C-Ni composites.

1.3 Scope of the Work

1) Mixing Fe-1.5Mo-0.5Mn-Si-C-Ni powder which have varied Nickel content of 0.50, 1.0, 1.50, 2.0 wt.% and 4 wt.% SiC.
2) Blending the powder mixture with powder blender machine with the rotation of 20-30 rpm to get a well-mixed powder.
3) Compacting the mixed powder into standard tensile bars and coin shape specimens according to MPIF standard 10.
4) Sintering the compressed tensile bars and coin shaped specimens at 1250℃ for 45 minutes under vacuum and then slowly cooled in the furnace.
5) Microstructure characterization and phase analysis of sintered Fe-Mo-Mn-Si-C-Ni composite specimens by optical microscope (OM), scanning electron

microscope (SEM), X-Ray Diffraction (XRD) and electron probe micro-analyzer (EPMA).

6) Mechanical properties investigation of sintered Fe-Mo-Mn-Si-C-Ni composite by Rockwell hardness test and tensile test.
7) Tribological analysis of sintered Fe-Mo-Mn-Si-C-Ni composite by pin on disc test.
8) Characterization of worn surfaces and wear debris of sintered Fe-Mo-Mn-Si-C-Ni composite by SEM.

1.4 Expected Benefits

The sintered Fe-Mo-Mn-Si-C-Ni composite which have higher volume fraction of ausferrite is expected to be successful via nickel (Ni) addition for applying in automotive applications and train brake lining of high-speed train with great mechanical properties and excellent tribological properties for long life cycle time.

CHAPTER 2

Literature Review

2.1 Powder metallurgy (PM)

Starting in 1920s, powder metallurgy (P/M) is introduced in the production of tungsten carbides and porous bronze bushes for bearings [8]. Nowadays, over 90% of powder metallurgy products are used in the transportation market because of sustainable technology, cost effectiveness and energy saving, reliable precision parts consistently which offer a high performance and greater flexibility of designing. Sintered parts can be produced with complex shapes and functions compared with traditional manufacturing methods such as extrusion, casting, stamping, forging, and machining. It is a unique powder manufacturing because it can produce new sintered parts which have higher mechanical properties to suit the specific application by diffusing based metal powders and other alloying elements such nickel, molybdenum, copper through the sintering and heat treatment processes [9]. Products made from high strength sintered material are shown in Figure 2.1. Sintered materials can be produced using any of the basic processes shown in Figure 2.2.

Figure 2-1 High strength sintered parts [10]

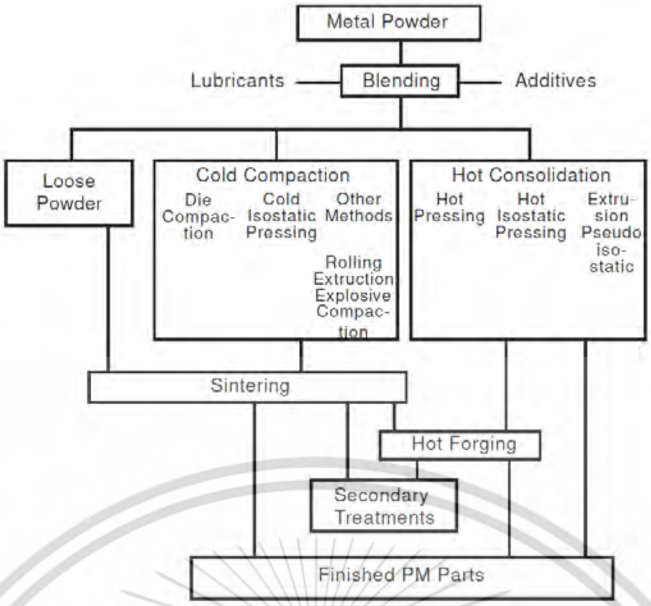

Figure 2-2 General P/M Processes [8]

2.1.1 Powder characteristics

Metal powders can be characterized by several parameters such as particle size and shape, particle distribution and particle density, specific surface area, and quality of mixing (segregation). The control of the powder composition influences the behaviour of the powder during compaction and sintering, and it also has significant effect on the microstructure, mechanical and tribological properties of the sintered parts. All of powder parameters influence are important for the powder density which referred to the mechanical properties of PM materials. The degree of densification (D_o) is a useful quantity that indicate the consolidation of powders which can defined as Equation 2.1. Where the ρ_a,express the apparent density, and ρ_s, is the density of the fully consolidated metal [8-11].

$$D_o = \frac{\rho_a}{\rho_s} \times 100 \qquad \text{2-1}$$

2.1.2 Powder Mixing

Powder mixing involves more than one type of powder, e.g., mixing solid lubricant or ceramic metals with a based metal powder. Occasionally, ceramic materials like silicon carbide are introduced, serving the dual role of lubrication and alloying, as seen with additives like zinc stearate and graphite in iron powder. To achieve optimal mixing efficiency, it is advisable to maintain a powder volume within the range of approximately 50% to 60% of the mixer's total volume. Furthermore, the mixing process necessitates careful consideration of rotation speed, which can vary from slow to high, and may involve human inspection of the mixed powder. The ideal mixing duration typically falls within the range of 30 minutes to 1 hour, with an optimum revolution rate of 20 to 40 revolutions per minute (rpm). However, these specific parameters can only be determined through practical experience with a given mixture in a particular mixer.

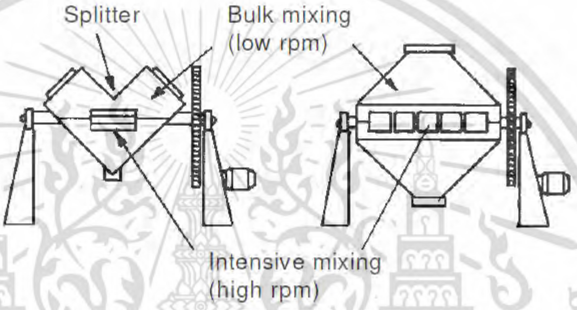

Figure 2-3 V-type and double cone mixers [8]

2.1.3 Powder Compaction

The major function of power compaction is to obtain mixed powder into mold and die, and compact to maintain required shape and size. Compacting is carried out with sufficient strength and density with hydraulic pressures. The operation of compaction must ensure that the green density is as uniform as possible, to achieve the maximum final product mechanical quality. The improvement of uniformity of the green density is apply the pressure from both ends . Figure 2.4 shows the schematic of tool set for compaction, it consists of upper punch, lower punch and die for pressing the powder to green specimen.

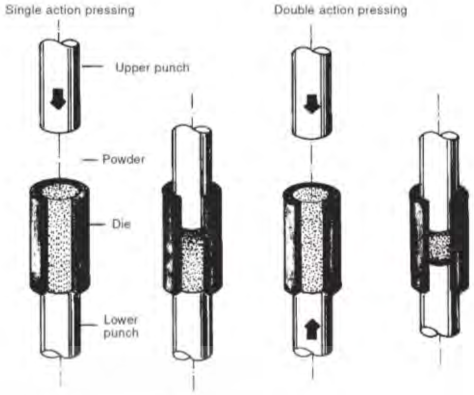

Figure 2-4 Single and double acting powder compaction [8]

2.1.4 Sintering

The sintering process is the process of heating to the temperature usually below the melting point for increasing structural integrity and strength of the green compact by the powder particles bonding. The potential for increasing the particle contact area and density during sintering is the reduction of the surface energy of the powder particles by the closure of pores between powder particles lead to a decreasing in the green compact total surface area. Not only the reduction of the surface energy is the necessary potential, but also diffusion mechanism leads to the increase in density. The diffusion mechanism can be defined as Equation 2.2, where D_o is the frequency factor, Q is an activation energy, T is the absolute temperature, and R is the universal gas constant. For each material, the activation energy and frequency factor are typical thermal constants. Therefore, increasing in density of powder compact is significantly dependent on the sintering [8-11].

There are generally three main stages in sintering. The initial stage is heating the specimen to evaporate or decompose the wax lubricant or binder that is added to the powder for easier compaction process. The intermediate stage is sintering stage, the sinter neck formation and merge between particle result in increasing of density and strength and progressed through atomic and particles diffuse as Figure 2.4. In this stage, the grain size is increased while the pore size shrinkage led to volume decreasing. The last is cooling stage, the cooling rate is depended on the final structure and mechanical properties needed [11].

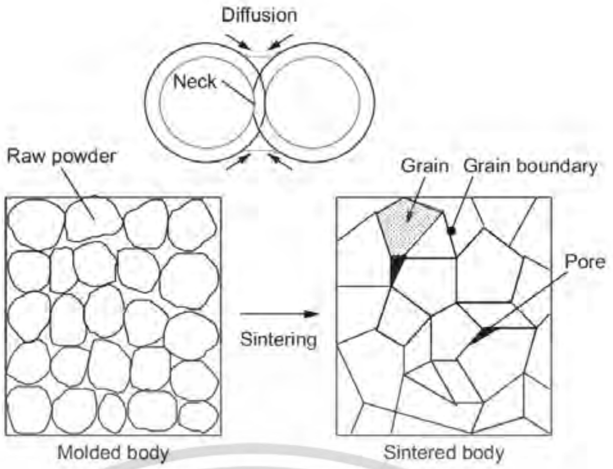

Figure 2-5 Schematic diagram of sintering process [11]

2.1.5 Sintering Temperature

The sintering process should be conducted under a good protective or vacuum atmosphere to prevent excessive oxidation of the powder surfaces. The heat for sintering is produced by hydrogen (H2), CO, and CO2 which can prevent the powder surfaces during sintering. Alternatively, nitrogen (N2) mixed with hydrogen atmospheres can be used. The influence of sintering temperature on the sintered density and time can be observed according to Figure 2.6.

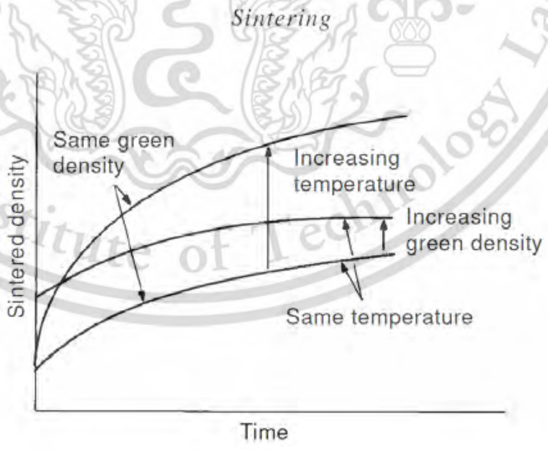

Figure 2-6 Sintered density time curves illustrating effects of increasing green density and sintering temperature on densification.

2.2 Alloying Element

Alloying element were added in base metals for changing the chemical composition with purpose to improve or adjust its material properties. While there are many alloying elements used to achieve various enhanced properties. Each alloying element has its own effect on the properties of materials.

2.2.1 Iron alloy phase diagram

Alloying elements can influence the equilibrium diagram in two ways: (i) by expanding the γ-field and encouraging the formation of austenite over wider compositional limits. These elements are called γ-stabilizer. (ii) By contracting the γ-field and encouraging the formation of ferrite over wider compositional limits. These elements are called α-stabilizers. The of alloying elements such as Ni, Mn, Co, Pt on the iron alloy phase diagram are as follows: (i) They can act as γ-stabilizers which promote austenite (γ) formation because they can broaden the γ-field by decreasing α-γ transformation and increasing γ-δ transformation (ii) and act as α-stabilizers which decrease the γ-field and promote ferrite formation.

When introduced in high enough concentrations, both Ni and Mn totally remove the bcc α-iron phase and replace it with the γ-phase at room temperature. Thus, Ni and Mn decrease Ae1 and Ae3 (Fig. 2.7 a). Ni and Mn are helpful components in austenitic steels because it is simpler to produce metastable austenite by quenching from the austenite zone to room temperature [12].

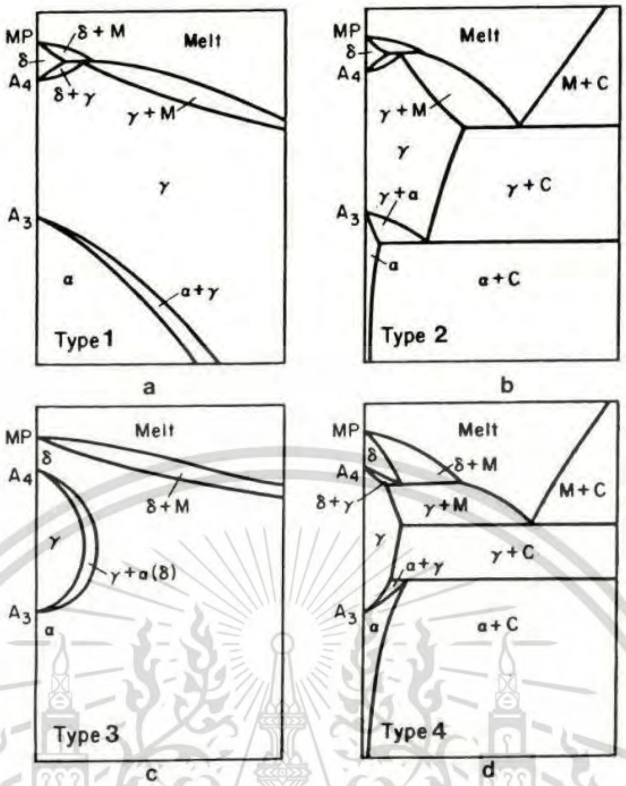

Figure 2-7 Iron alloy phase diagrams: (a) open γ –field; (b) expanded γ – field; (c) closed γ –field; (d) contracted γ –field [12]

2.2.2 Effect of alloying element on the formation of alloy carbides (Secondary hardening)

In the secondary hardening process of material which adds the alloying element such as Cr, Mo, V, and W, the carbides in coarse cementite dispersion are replaced by a finer alloy carbide dispersion, results in higher hardness. Figure 2.8 shows the effect of molybdenum on hardness of secondary hardening. The results show higher hardness value while increasing percent of molybdenum.

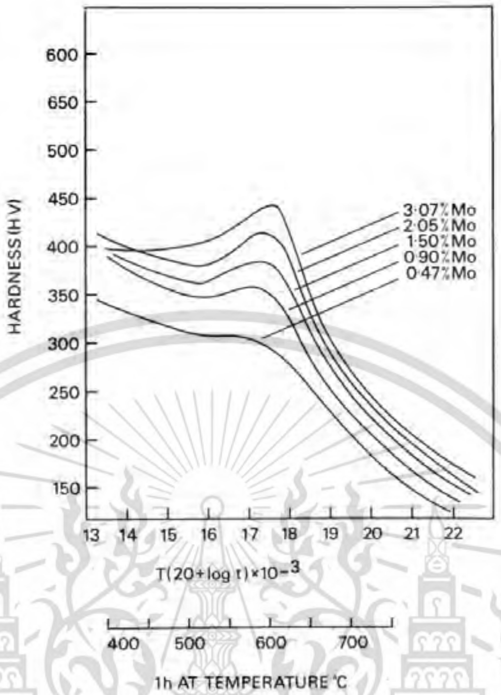

Figure 2-8 The influence of Mo on the tempering of quenched 0.1wt% C steels

2.2.3 Effect on ferrite hardness

The hardness value of ferrite is also affected by the formation of solid solution. The solid solution is produced by additional alloying element in base metal. Figure 2.9 shows the effect of substitutional alloying element additions on hardness of ferrite. The results show that hardness increase caused by substitutional solution. Si and Mn element gives high hardness increase, on the other hand, Cr show the smallest relatively effect on hardness of ferrite [12].

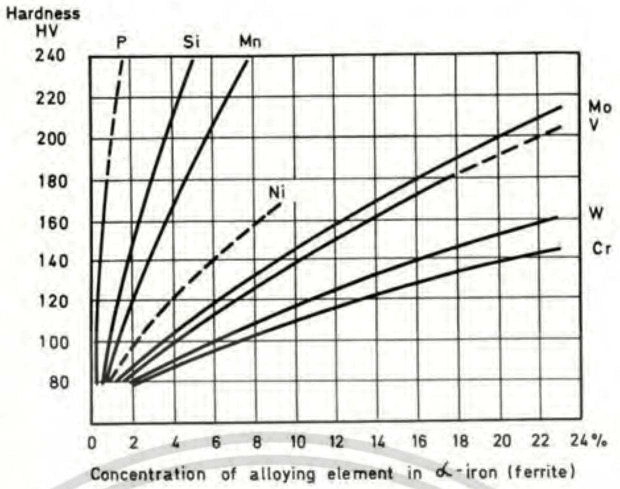

Figure 2-9 Influence of alloying element on ferrite hardness

2.3 Self-lubricant material

There are various types of solid lubricants such as graphite, molybdenum disulfide (MoS2), zinc, copper, and boron nitride (BN). Solid lubricants are used where the containment of liquids is a problem because liquid lubricant can oxidize and decompose when performed at high temperature leading to decreasing in its efficiency and performance. On the other hand, self- lubricant or solid lubricant can utilize lubrication at various conditions [11].

2.3.1 Graphite

Graphite is a solid lubricant which has a hexagonal crystal structure. The crystal structure of graphite consists of thin parallel planes (graphene) which bonded by weak Van der Waals forces to each other. Each carbon atom of graphene is bonded by a strong covalent bond to three other atoms with an angle of 120°. The weak bond between the graphene causes easily shearing of the planes toward the direction of the force. The graphene that released from graphite crystals by lamellar displacement create graphite films on surfaces results in lower coefficient of friction. However, application of graphite in practical is limited at high temperature because of oxidation. But additives composed of inorganic compounds can be added to enable use. Graphite in cast iron can take several forms, such as flakes of various sizes and distributions in gray cast iron and nodules in ductile cast iron as shown in Figure 2.10.

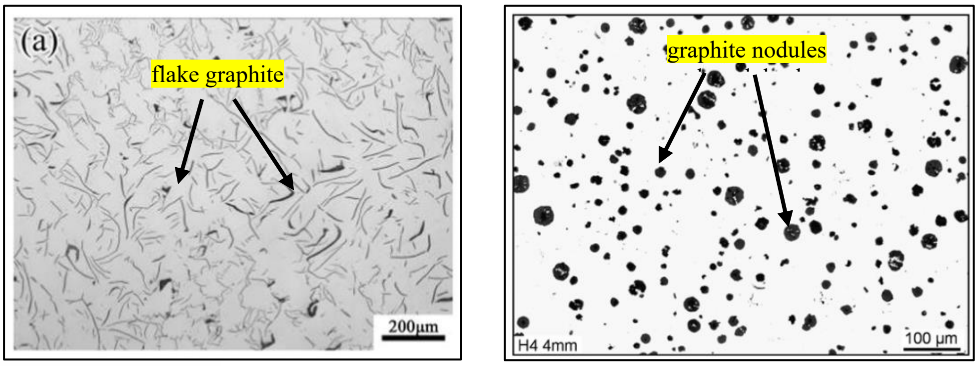

Figure 2-10 (a) flake graphite in grey cast iron [13], (b) graphite nodules in ductile cast iron [14]

2.4 Microstructure

The resulting microstructure in sintered alloys can vary depending on the composition of the alloy, sintering temperature, pressure, and time. The typical microstructures of sintered alloys include granular or grain-like microstructure, pores, phase distributions, inclusions and defects, and second-phase particles such as carbides or intermetallic compounds. It can strongly influence the properties of the material such as strength, ductility, toughness, corrosion, hardness, wear resistance. Figure 2.11 shows hardness of various microstructure of steels containing up to 1.2wt.% carbon. Martensite demonstrates the highest hardness, while hardness of tempered martensite and bainite are slightly lower. However, pearlite and ferrite show significantly lower hardness, whereas ferrite and spheroidized carbide indicated the lowest hardness compared with others.

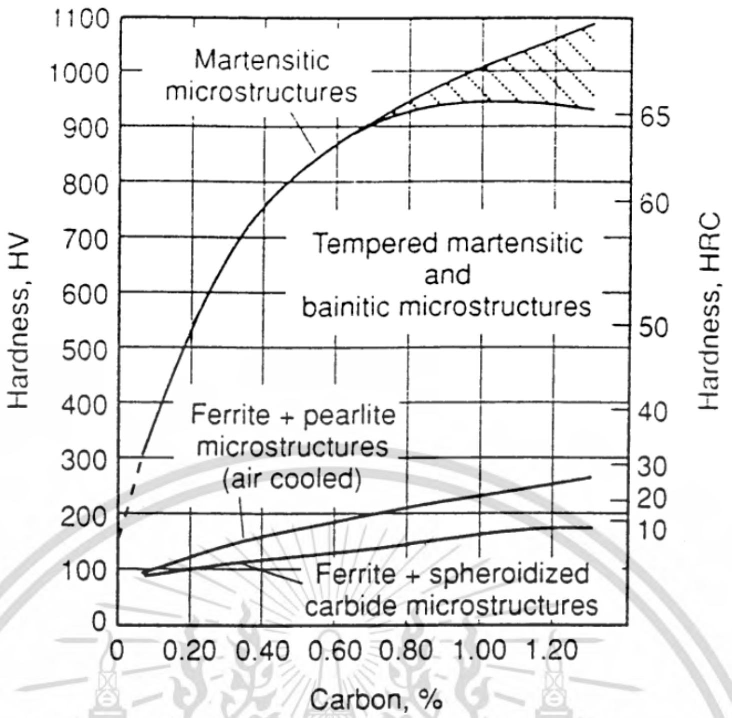

Figure 2-11 Hardness of various microstructure of steels containing up to1.2wt.% C [15]

2.4.1 Ferrite

Ferrite is a crystalline phase of iron that has a body-centered cubic (BCC) crystal structure. It is the purest form of iron and exists at temperatures below 912°C (1,674°F) in the iron-carbon phase diagram. The solubility of carbon atom in ferrite phase is very low, maximum soluble is 0.022% at 727℃ and 0.008% at room temperature. This phase has low dislocation motion resistance due to its crystal structure, which effect to low in its strength. Ferrite is magnetic and is commonly found in low-carbon steel, particularly at room temperature. It has good ductility and is relatively soft compared to other phases like martensite. Figure 2.12 illustrates the micrograph of ferrite microstructure.

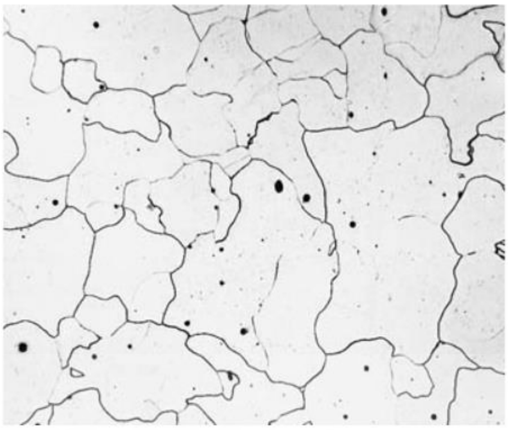

Figure 2-12 The optical micrograph of ferrite microstructure in low carbon steel

2.4.2 Pearlite

The formation of pearlite occurs during the slow cooling of an initially austenitic (FCC) crystal structure in iron-carbon alloys, typically in the eutectoid steel composition, which contains about 0.76% carbon. Pearlite consists of fine metastable lamellar structures of that mixed of ferrite, and cementite (Fe_3C) which forms at temperatures below the lower critical temperature. Under proper temperature, cementite can transform to graphite. The distance layer between ferrite and cementite is known as the interlamellar spacing [16]. The mechanical properties such as hardness of a fully pearlitic steel vary with the interlamellar spacing. Slower cooling rates tend to produce finer pearlite structures (Figure 2.13a), while faster cooling rates may result in coarser pearlite(Figure 2.13b) or other microstructures which have lower hardness.

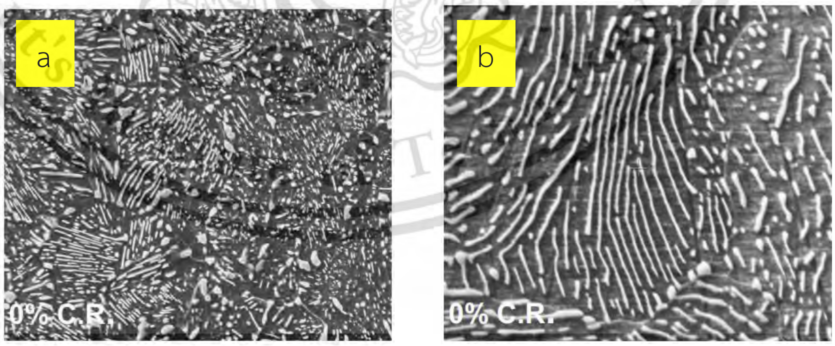

Figure 2-13 SEM micrographs of (a) fine pearlite (b)coarse pearlite in eutectoid steel [17]

2.4.3 Ausferrite

Ausferrite is a microstructure that forms in iron-carbon alloys like pearlite but due to its excellent combination of strength and ductility, it is a desirable microstructure for certain engineering applications. Ausferrite is a mixture of both austenite and ferrite. The formation of ausferrite(Figure 3.14) occurs during austempering of an initially austenitic (FCC) crystal structure in iron-carbon alloys followed by the slow cooling. The ausferrite microstructure is comprised of two primary phases known as bainitic ferrite and austenite. Bainitic ferrite forms as a coarse structure or fine needle-like/acicular structure within the microstructure. The ausferrite microstructure can be distinguished into upper ausferrite and lower ausferrite. Upper ausferrite has coarse bainitic ferrite plates which provides excellent strength and toughness, while lower ausferrite has fine acicular bainitic ferrite and high C austenite which provides excellent ductility and elongation.

High Carbon Austenite (HCA): The remaining austenite in the microstructure, which did not transform into martensite during the quenching step, transforms into high carbon austenite during the austempering process. This phase is relatively stable and provides ductility.

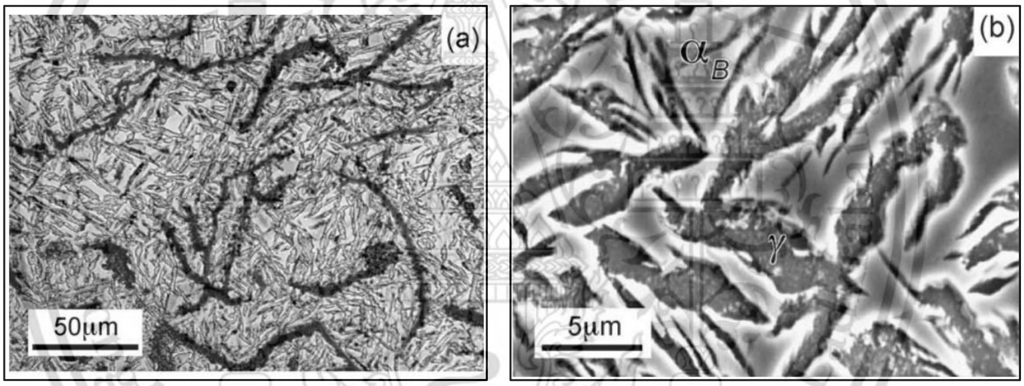

Figure 2-14 OM image of ausferrite containing bainitic ferrite and austenite [18]

2.5 Ductile cast iron or nodular cast iron

Ductile cast iron or nodular cast iron has a microstructure consisting of spheroidal graphite particles or nodules embedded in a matrix of ferrite and pearlite. The ferritic-pearlitic matrix consists of ferrite halos around the nodules and pearlite away from them, giving the so-called bulls-eye structure illustrated in Figure 2.15. Formation mechanisms can be divided into two parts such as ferritic reaction and pearlitic reaction. The ferritic reaction, which occurs with the growth of ferrite, is the diffusion of carbon from the residual austenite to graphite nodules via the ferrite halos. In the metastable system known as the pearlitic reaction, the temperature can drop to a point where pearlite can nucleate and develop if the material is slowly cooled [19].

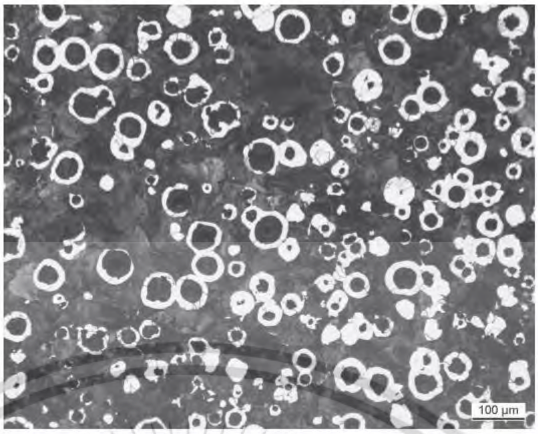

Figure 2-15 Bulls-eye structure of ductile cast iron or nodular cast iron [19]

2.5.1 Austempered Ductile Iron

Austempered ductile iron goes through the isothermal heat treatment process known as 'austempering' at temperatures between pearlite and martensite phase (Figure 2.16). The duration of the austempering process must guarantee that enough bainite ferrite is formed to allow the carbon-containing austenite that remains to be mostly kept at normal temperature.

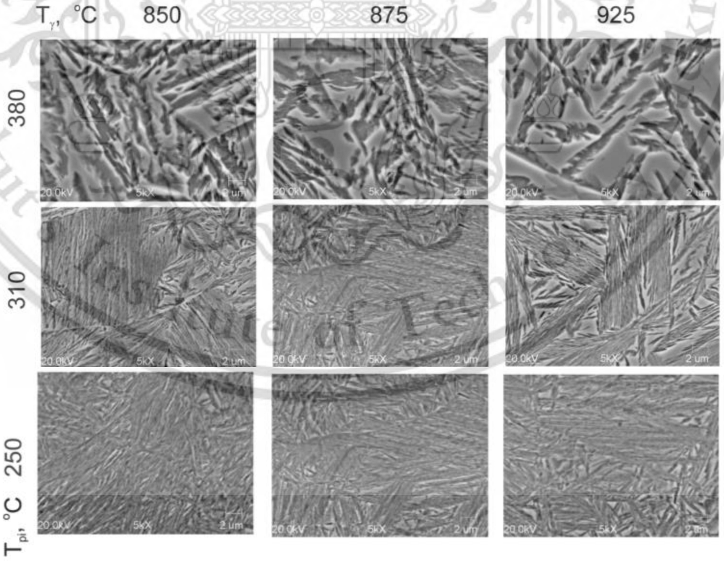

Figure 2-16 SEM micrograph of ductile iron at different austempering temperatures [20]

2.5.2 Fe-Mo-Si-C sintered composite with austempered ductile iron microstructure

Sintered alloys with the composition of Fe-0.85Mo powder+ 4.0 wt.% SiC and Fe-1.50Mo powder + 4.0 wt.% SiC was produced via the 'press and sinter' process. It was observed that sintered Fe-Mo-Si-C composites have ferrite-pearlite ductile iron microstructure which is black particles, ferrite halos and pearlite/bainite shells as shown in Figure 2-17. The process described as "onion-like" was responsible for the lower carbon solubility in γ-phase, which led to a fracture that was frequently seen along the border between the Si-based core and graphite shell [21].

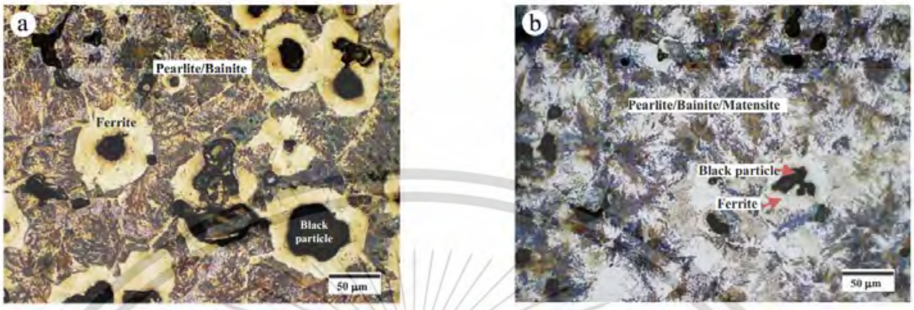

Figure 2-17 Microstructure of Fe-Mo-SiC alloys (a) 0.85Mo (b) 1.50Mo

2.5.3 Fe-Mo-Si-C composite with varied Mo content

Four sintered alloys with compositions of Fe-Mo-1.5Mn powder + 4wt.%SiC where Mo has varied content of 0.0, 0.5, 0.85, 1.50 wt.% was produced with ‘press and sinter’ process [21-22]. All experimental sintered composite exhibited black particles, ferrite grains in the form of halos around black particles, pearlite, bainitic ferrite (BF) and martensite-austenite (MA) structures. In 0.85Mo and 1.50Mo sintered composites, BF/M-A structure with no carbide precipitation was observed. It was found that a special microstructural feature called ‘ausferrite’ consisting of ferrite and austenite coexisted with ferrite and pearlite in sintered Fe-Mo-Si-C composites with Mo contents of $\geqslant$ 0.85 wt.% illustrated in Figure 2.18c-d.

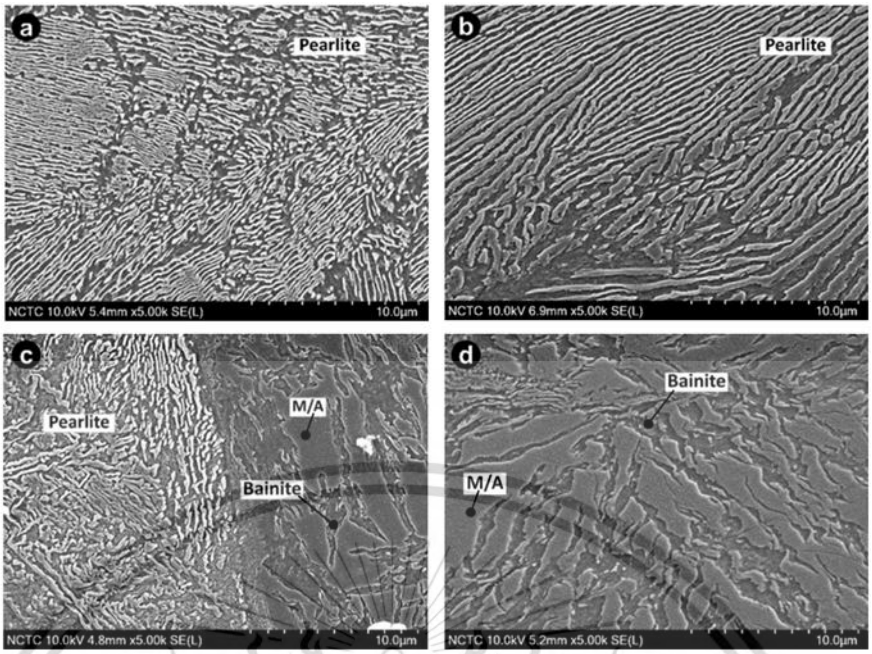

Figure 2-18 SEM micrographs of sintered composites (a) 0.00Mo, (b) 0.50Mo, (c) 0.85Mo, and (d) 1.50Mo [22].

2.6 Green Density

In sintered composite materials, the green densities were lower than sintered densities because of densification of particle bonding. Green density is the ratio of external and metal powder volumes before being sintered which indicates how the powder particles are packed together. Powder compacts of high green density led to achieve densification during sintering because green density improvements may also be affected by employing smooth and regularly shaped annealed particles with high particle densities.

During the sintering process, each powder particle was bonded together. The particles do not really melt because the temperature does not reach melting temperature, but rather neck is formed on the contacting areas at elevated temperatures. Due to sintered neck growth, the pores were filled, cause densification and shrinkage of the component, then the void spaces between the powder particles were removed [23-24]. Sintered density increased with increasing sintering temperatures and the amount of time spent at temperature. Commonly, the increasing of the isothermal holding time will result in the decreasing of open porosities of all the sintered alloys (Figure 2.19). However, further increasing the isothermal holding time has a limited effect on eliminating the open porosities [25-26]. While the specimen was heated, the size of the specimen was reduced along with the porosity size. Hence, higher temperatures and longer sintering will form the particle better bonds.

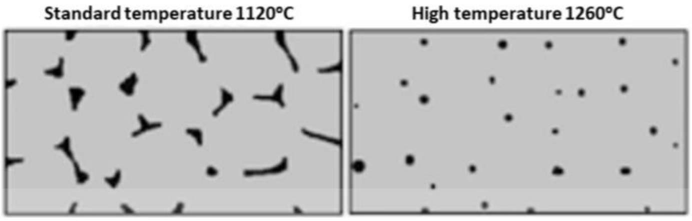

Figure 2-19 The particles bonding at difference temperature.

2.7 Tribological Test

Wear testing is performed to determine the number of materials removed, to investigate the wear mechanism and predict the wear performance of a component after a period in-service. The wear properties can be determined by various way such as mass loss, volume loss, the geometry and size of wear debris, the character of worn surface, and type of wear. Wear measurement can be done in a common technique using precision digital balance to measure the mass loss. The microscope was also used for measuring the wear depth and cross section area of a wear track to define the wear volume loss. The wear testing is performed to evaluate the wear properties to investigate whether material is appropriate for a specific application of wear, to select the proper surface and material to reduce wear, and to determine the effect of treatment conditions on the wear properties and mechanism. There is various type of wear test such as a rolling sliding wear tester, an abrasive wear tester, and a pin on disc wear tester.

ef

2.7.1 The pin on disc wear tester

The pin on disc test is commonly used to determine the wear properties because of the economic cost, short testing period, and easy to access [27]. The schematic of pin on disc wear tester is shown in Figure 2.20. The pin on disc tester machine consists of a pin with various geometry, which attached with the precise weight at a specified load. The most popular geometry of the pin is cylindrical and spherical due to the uniform loading. The pin on disc wear testing is carried out to evaluate friction and wear properties of materials under sliding condition in relative motion. Commonly, the tests are performed under various testing standards such as

ASTM F732, ASTM G133, and ASTM G99. While testing was performed, the normal load is transferred from pin to the contacting surface results in wear mechanism on pin and surface of tested specimen. The temperature, wear and friction force are continuously monitored during the test which can be converted to the tribological properties such as Friction coefficient (COF), wear rate, and wear resistance.

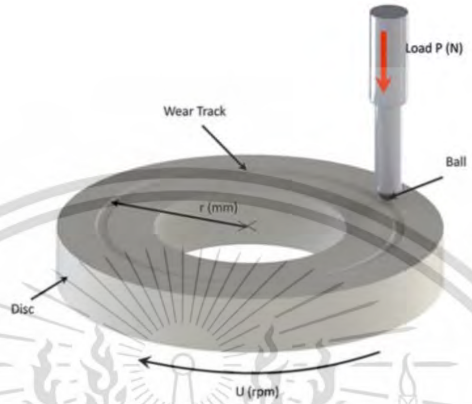

Figure 2-20 The schematic of pin on disc wear tester.

2.7.2 The friction coefficient

The friction coefficient (μ) obtained from the wear test, which indicate the ratio of the friction force and the normal applied load between two counterpart specimens. The equation 2.2 expresses the friction coefficient equation, where f is defined as friction force and load defined as normal applied load. Figure 2.21 presents the typical curve of friction coefficient and time [28]. It shows two sections of COF, the transition section and the steady state section. The transition section is attributed to the run-in state. During the run-in state, some chemical reactions occur, and the surface roughness changes until the system comes to a steady state. The second section is called steady state because the friction coefficient in this state is already stable. The steady state may either decrease or increase from the run-in state, depend on the types of material contact and parameters of contact pairs.

$$\text{Friction Coefficient } (\mu) = f/Fload \qquad 2\text{-}2$$

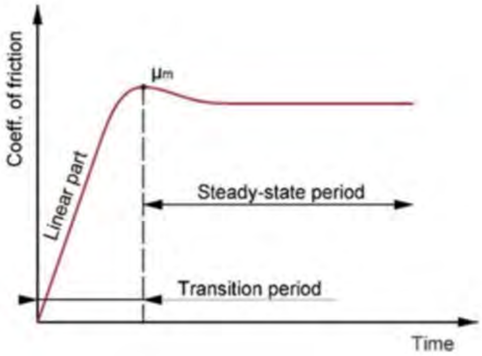

Figure 2-21 The typical curve of friction coefficient and time

2.7.3 Wear rate

Wear rate can describe the material removal per unit sliding distance or time by reflecting mass loss, volume loss or linear dimension change. The common unit of wear rate is m3/m or mm3/mm.

2.7.4 Mass loss

Mass loss is a mass difference between initial mass and final mass which is caused from wear. Mass loss obtained by precision digital balance measurement, which is the convenient method for wear measurement, especially when the worn surface is irregular shape. Before the weight measurement, the specimen must be carefully cleaned. The common unit of mass loss is gram (g) and milligram (mg).

2.7.5 Volume loss

Volume loss is one of the factors that can describe the wear behavior. Normally, volume loss calculated from length and width of wear scar track, or scar profile according to the geometry of the wear track. The measurement of width and length of wear scar track can be performed by a microscope. The common unit of volume loss is mm3, mm3/m, mm3/N, and mm3/N.m. Volume loss is recommended comparison of wear among materials with different densities. However, this method is inappropriate for an irregular wear track.

2.8 Wear mechanism

The wear mechanism is the removal of solid material from surface and/or subsurface when two solid surfaces are in tribological contact due to the moving components. Tribological contacts are influenced by many properties and environment such as hardness, surface of materials, surface roughness, normal load, type of motion, humidity, temperature, and lubricant properties. The wear mechanism can be characterized as severe and mild wear. The worn surfaces with smooth and small wear debris size not over about 1µm is characterize as mild wear. On the other hand, the roughened worn surface with a large wear debris size which can be observed by naked eye can defines as severe wear. The large amount of wear results in low life service time of the components. Thus, the components life cycle time can be developed mainly in two ways which is applying a lubricant and surface modification [11]. The important wear mechanisms can be categorized into adhesive wear, abrasive wear, delamination wear, and corrosive wear.

2.8.1 Adhesive wear

Adhesive wear occurs from shearing of adhesive bond (cold welds) of asperities lead to transferring of material from one surface to another surface as Figure 2.22. The cold welded of asperities is resulted from plastically deformed and welded under high temperature and load in relative motion. When considerate at the contact points, the cohesive bond of the weaker material is weaker than the adhesive bond of welded asperities.

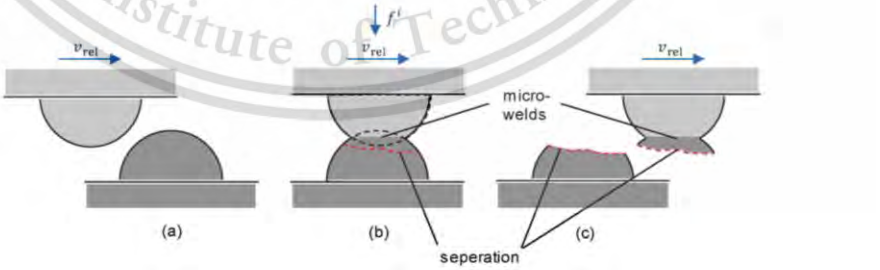

Figure 2-22 Schematic of adhesive wear mechanism.

2.8.2 Abrasive wear

Abrasive wear is damaging of surface by plastic deformation or fracture which occur from asperities of a rough, hard particles or hard surfaces sliding along a softer solid surface. The character of damaging is wedging, cutting, and ploughing phenomena.

Ploughing is a groove on the surface of material. Abrasive wear can categorize by mainly in two modes of wear that is two body abrasive wear and three body abrasive wear. Figure 2.23a show the schematic pattern of two body abrasive wear which is a simple form of abrasion. It's caused by the difference in degree of surface roughness and hardness of two solid rubbing surfaces. Hard abrasive particles are formed by fracture and severe abrasion. However, it can be improved by reducing surface roughness and applying lubrication. Figure 2.23b show the schematic pattern of three body abrasive wear. The abrasive particles between contact area are slide and roll on the surface, which results in cutting wear [29] and localized plastic deformation in relative motion of the contact surface [30]. The detail mechanism also depends on the gap between the two main bodies and the particle size [31–33].

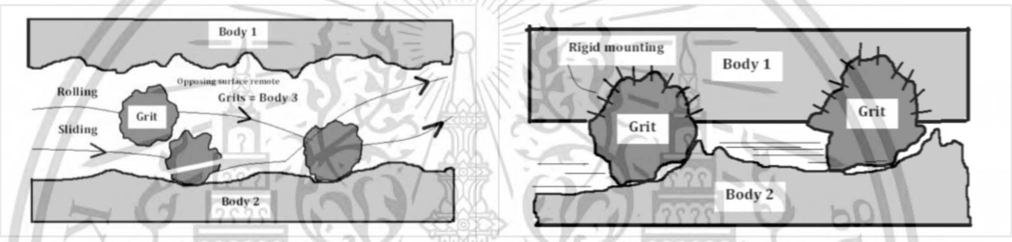

Figure 2-23 Schematic illustration of (a) two body abrasive wear mechanism and (b) three body abrasive wear mechanism

2.8.3 Fatigue/ Delamination wear

Delamination wear is caused by fatigue from the cyclic loading. During the cyclic loading, some crack is present on surface or subsurface. Then, the surface cracks propagate and connect with other cracks. Results in generating wear particles in flake-like sheets and pits or voids formation on contacting surface. The propagation of crack can be influence by the relative humidity in the air, in the high moisture atmosphere, the crack propagate occurs rapidly when compare with dry atmosphere [11], [34]. Figure 2.24 and 2.25 present the SEM micrograph of severe delamination wear and mild delamination wear, respectively.

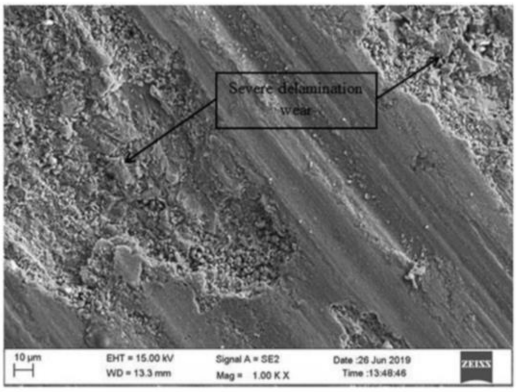

Figure 2-24 SEM micrograph of severe delamination wear.

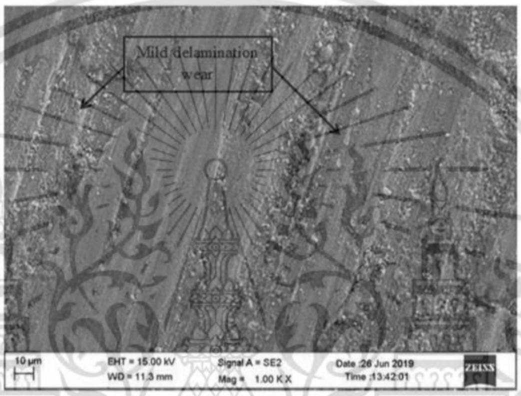

Figure 2-25 SEM micrograph of mild delamination wear.

2.8.4 Corrosive/ Oxidative wear

Corrosive or oxidative wear can occur when the oxygen or other gases have a reaction on the sliding surfaces results in intense damage and material losses. Sometimes oxidative wear can be generated by the anti-wear or other chemical additives because of the presence of dissolved oxygen. The oxidation rate at the beginning is fast because the oxide film grows quickly on the relative surface. When the oxide film thickness on the surface reaches about 3-4 nm, the oxidation rate on the surface decreases and the oxide film continues to form by oxygen diffuse into the metal [11-35]. Figure 2.26 and Figure 2.27 present the schematic of oxidative wear mechanism [36] and SEM micrograph of oxidative wear.

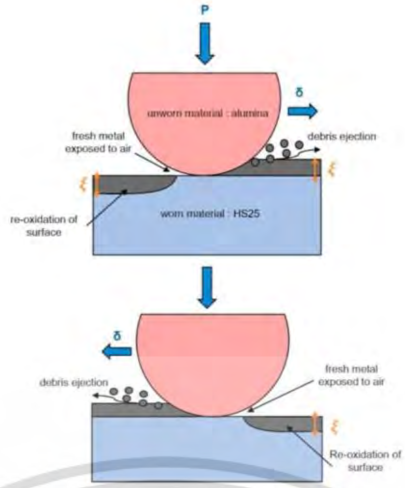

Figure 2-26 Schematic of oxidative wear mechanism.

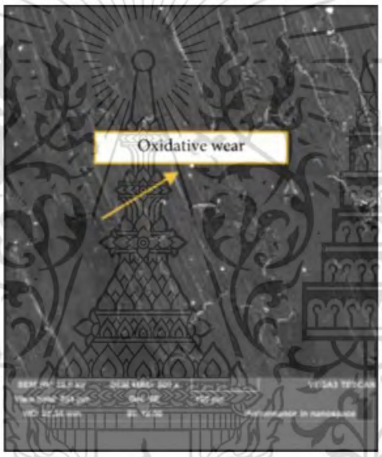

Figure 2-27 SEM micrograph of oxidative wear.

CHAPTER 3

RESEARCH METHODOLOGY

3.1 Materials

3.1.1 Pre-alloyed Fe-Mo-Mn powder

Sintered Fe-Mo-Mn-Si-C-Ni composites were prepared from pre-alloyed Fe-Mo-Mn powder as in Figure 3.1, Fe-1.50Mo-0.15Mn, namely ATOMET 4901. This pre-alloyed Fe-Mo-Mn powder is designed for a highly compressible, water-atomized alloy steel designed for use in high performance powder metallurgy, high strength, and sinter hardening applications.

Figure 3-1 Iron based particle powder.

3.1.2 Silicon carbide

Figure 3.2 shows the silicon carbide powder (Si-C) which frequently employed as the reinforcing phase in iron-based alloys because of its high strength and chemical stability, especially in severe environments. Moreover, it is used to reduce fiction coefficient and mechanical interactions between surfaces in relative motion. Its physical properties have average particle size lower than 40 µm (as received).

Figure 3-2 SiC powder

3.1.3 Zinc stearate

Zinc stearate is added as a lubricant or binding agent during mixing of iron powder or other metallic based composites before compaction for enhances blending properties and improve flow with powdered metal and imparts consistent porosity for fabrication of self-lubricating components. In addition, it prevents the parts from adhering to the mold in compaction process and leaving a better finish. Figure 3.3 show the zinc stearate powder.

Figure 3-3 Zinc stearate powder

3.1.4 Argon gas

Argon gas, show in Figure 3.4, were used to prevent chemical oxidation on the surface of sintered parts. Because Argon gas can remove oxygen from air before and after sintering process.

Figure 3-4 Argon gas cylinders.

3.1.5 Nital etchant

Nital etchant as shown in Figure 3.5 is a mixture of nitric acid and alcohol commonly used for etching low carbon steels to reveal the microstructure of the metal through selective chemical attack. Etchants will preferentially attack high energy sites, such as boundaries and defects.

Figure 3-5 Nital etchant

3.2 Experimental Equipment

3.2.1 Digital balance

Laboratory Digital balance 3-digit is used for Lab weighing and density calculation. It is defined by high levels of accuracy and precision in analytical testing. Figure 3.6 shows the Digital balance (3-digit).

Figure 3-6 The Digital balance (3-digit)

3.2.2 Analytical balance

Analytical Digital balance 4-digit is used for Lab Weighing and wear analysis. It defined by high levels of precision, strong environmental adaptability and readability at 0.0001g. Figure 3.7 shows the Analytical balance.

Figure 3-7 The Analytical balance (4-digit)

3.2.3 Powder blender

Powder blender as shown in Figure 3.8 is uses for mixing of the metal and additive powders in different area type together, operate using a rotating powder bottle at desired revolution per minute.

Figure 3-8 Powder blender

3.2.4 Hydraulic pressing machine

The hydraulic pressing machine with load 100 Ton as shown in Figure 3.9 is used to compact mixed powder into a green product with vary shape depend on mold and die by using the hydraulics pressure.

Figure 3-9 Hydraulic pressing machine

3.2.5 High vacuum sintering furnace

High vacuum sintering furnace offered by SCHMETZ D59708 MENDEN as show in Figure 3.10 is used for sintering the specimens under the vacuum atmosphere. After the sintering process, the specimen becomes the green density material. The sintering process directly affects grain boundary shape, pore size, the grain size, and distribution in the microstructure, which affects the material properties.

Figure 3-10 High vacuum sintering furnace SCHMETZ D59708 MENDEN

3.2.6 High precision cutting machine.

High precision cutting machine which is Discotom-5 cut off machine as Figure 3.11 is used to cut materials into specific shapes to prepare specimen for microstructure characterization.

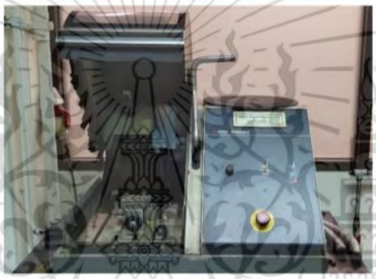

Figure 3-11 High precision cutting machine.

3.2.7 Hot mounting press

Hot mounting press as Figure 3.12 is used to prepare the sample before grinding and polishing. The aim of mounting is to handle odd shapes or small size of specimens and to protect coating or thin layers, provide good edge retention as well as to handle fragile materials, during preparation. In hot mounting process, the specimen is mounted under pressure and heat with a hot mounting press machine.

Figure 3-12 Hot mounting press

3.2.8 Metallurgical Grinding Polishing Machine

The Labopol-5 machined as Figure 3.13 is a Metallurgical Grinding Polishing Machine which used for sample preparation process by grinding and polishing with high reliability of rotational speed, the goal being to produce a good surface finish. with no scratch, no deformation, and highly reflective sample surface.

Figure 3-13 Metallurgical Grinding Polishing Machine

3.2.9 Silicon Carbide paper

Silicon Carbide paper (SiC paper) grit size 120, 180, 240, 400, 600, 800, 1000, and 4000 as in Figure 3.14 are used for grinding metallic specimens to remove the surface layers damaged and achieve a smooth, flat and without scratch surface for microstructure characterization.

Figure 3-14 Silicon Carbide paper

3.2.10 Polishing cloth

Micron polishing cloth as Figure 3.15 is use after grinding step to remove the scratches which were produced from the grinding step. The objective of polishing step in specimen preparation is a smooth and reflective surface by removing the last thin layer of the deformed metal.

Figure 3-15 Micron polishing cloth

3.2.11 Diamond suspension

The Diamond suspension size 6, 3 and 1 μm are show in Figure 3.16, use in sample preparation step with polishing cloth for produce fast removal and to generate a perfect polished surface which ready for analysis. The diamond suspension type to use depends on the surface finish required and the material type.

Figure 3-16 Diamond suspension size 6, 3 and 1 μm

3.3 Characterization instruments

3.3.1 Digital vernier

Digital vernier as Figure 3.17 is a precision instrument to measure the internal and external dimensions of an object by displays the reading as a numeric value.

Figure 3-17 Digital vernier

3.3.2 Macro hardness testing machine

The macro hardness testing machine offered by Instron-930 is shown in Figure 3.18 which is an equipment for measuring the hardness of the macro structure by conventional Rockwell hardness testing with high precision tester and quick results. In the Rockwell test, results are directly and rapidly obtained without the need for a secondary, dimensional measurement requirement which reduces human error.

Figure 3-18 Instron-930 Macro hardness testing machine

3.3.3 Universal testing machine (Instron 8801)

A Universal Testing Machine by Instron 8801 Universal Instrument, show in Figure 3.19, is used to evaluate the tensile properties of materials in this research. This testing equipment can define materials properties such as plastic deformation, strain hardening, elasticity, yield strength and tensile strength.

Figure 3-19 Instron 8801 Universal Instrument

3.3.4 Optical Microscope

Optical Microscope (OM) by Olympus STM7, Japan, show in Figure 3.20, is a type of microscope that uses visible light and a system of lenses to magnify images of small samples such as microstructure of specimens in this research. Optical microscopes were commonly used and easy to develop because they use visible light, so samples can be directly observed by the naked eye.

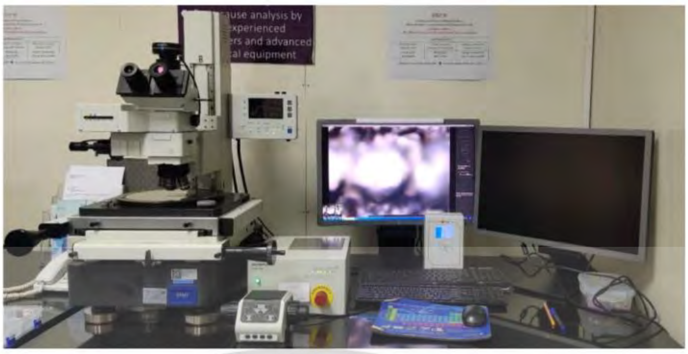

Figure 3-20 Optical microscope by Olympus STM7, Japan

3.3.5 Scanning Electron Microscope

Scanning Electron Microscope (SEM) by Hitachi SU8230, Japan, show in Figure 3.21, is used to investigate microstructure of specimens, the worn surface, wear debris and counter ball surface in micro scale. SEM scans were operated by focused electron beam over a surface to create an image. The focused electrons beam is interacting with the sample, then they produce secondary electrons, backscattered electrons, and characteristic X-rays. These signals are detected and collected by detectors to generate images which are displayed on the computer screen.

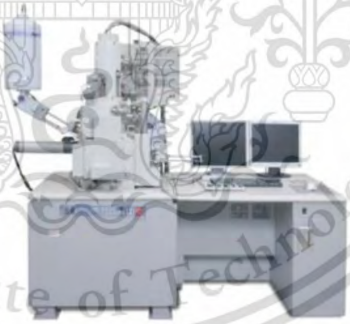

Figure 3-21 Scanning electron microscope by Hitachi SU8230, Japan

3.3.6 X-Ray Diffraction Analysis

X-Ray Diffraction Analysis (XRD), show in Figure 3.22., is used to identify phase of crystal and crystal orientation and reveal information of chemical composition which present in a specimen. Identification of phases is achieved by comparison of the reference databases which acquired data of material.

Figure 3-22 X-Ray Diffraction Analysis

3.3.7 Pin-on-disc testing machine

Pin-on-disc testing machine is carried out according to ASTM G99, show in Figure 3.23 is used to evaluate friction and wear characteristics in sliding contacts. Sliding occurs between a rotating disc and a stationary pin. Wear track diameter and normal load can be varied. Electronic sensors are used for monitoring tangential frictional force and wear.

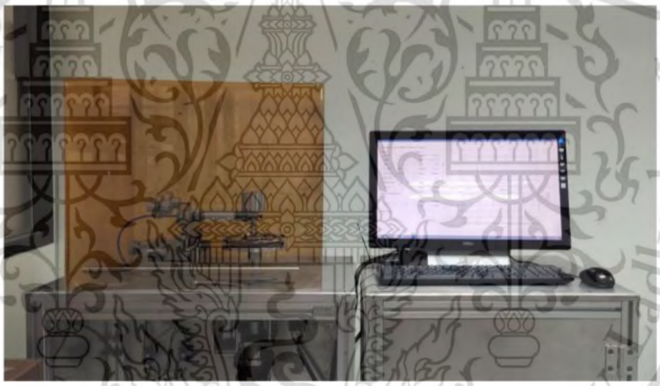

Figure 3-23 Pin-on-disc testing machine (ASTM G99)

3.4 Experimental procedure

3.4.1 Mixing powder

Sintered Fe-SiC alloy was prepared as a reference material from pure Fe powder mixed with fixed 4 wt. % silicon carbide powder. And the experimental sintered Fe-Mo-Mn-Si-C alloys were prepared from 3 different pre-alloyed Fe-Mo-Mn powders, namely Fe- 0.50Mo-0.15Mn, Fe-0.85Mo-0.15Mn and Fe-1.50Mo-0.15Mn, mixed with fixed 4 wt. % silicon carbide powder. The powders were mixed with 1 wt.% Zinc stearate in powder mixer with speed 6.5 RPM for 1 hour. The chemical composition of mixed powder is given in Table 3.1.

Table 3-1 The chemical composition of mixed powder

Sintered Composite	Base metal powder	SiC (wt.%)	Nominal composition (wt. %)					
			C	Si	Mo	Mn	Ni	Fe
00Ni	Fe-1.5Mo-0.15Mn	4.0	1.20	2.80	1.44	0.14	0.00	Bal.
05Ni	Fe-1.5Mo-0.15Mn	4.0	1.20	2.80	1.43	0.14	0.50	Bal.
10Ni	Fe-1.5Mo-0.15Mn	4.0	1.20	2.80	1.43	0.14	1.00	Bal.
15Ni	Fe-1.5Mo-0.15Mn	4.0	1.20	2.80	1.42	0.14	1.50	Bal.
20Ni	Fe-1.5Mo-0.15Mn	4.0	1.20	2.80	1.41	0.14	2.00	Bal.

3.4.2 Compaction

The standard tensile test bars conforming to the MPIF standard 10, ASTM B783 (Figure 3.24) with green density of 6.5 ± 0.01 g/cm3 were prepared from mixed alloy powders by using 100 ton hydraulic pressing machine. The disk specimens for tribological tests were prepared under the same conditions with the tensile test bars and the dimensions of disk specimen are shown in Figure 3.25. To reduce the effects of back pressure produced, each specimen was kept in die under pressure for 10 seconds.

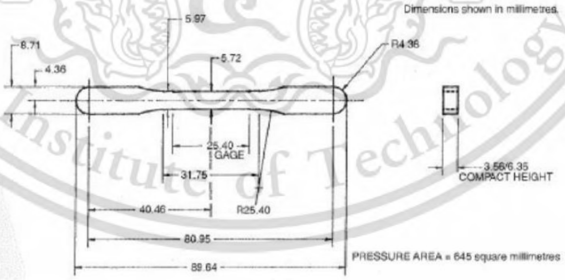

Figure 3-24 The standard tensile test bars (MPIF standard 10, ASTM B783)

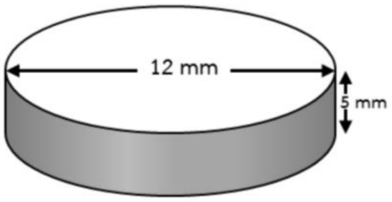

Figure 3-25 Dimensions of disk specimen

3.4.3 Sintering

The green compact both standard tensile test bars and disk specimen were sintered in a high vacuum sintering furnace because it commissioned a high temperature and reduction in oxidization. The sintering profile was performed in three stages as shown in Figure 3.26 under vacuum atmosphere. The first stage of sintering was heating up to 600℃ to de-waxing temperature for 60 minutes to remove lubricant, binder, other organic materials from the specimen improves integrity of compacts for sintering process. Next, heating up to 1250℃ to sintering temperature and keep these temperature for 45 minutes to complete the phase stability (homogenize) of the material (all area of specimen is change to austenite phase). The last step of sintering was slowly cooling inside the furnace. The density of sintered specimen was measured according to MPIF standard 42.

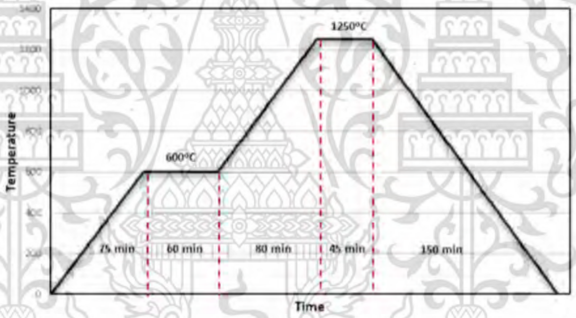

Figure 3-26 The sintering profile.

3.5 Mechanical test

3.5.1 Hardness test

For macro-hardness, five samples of sintered tensile test bars were used for each condition and a total of five conditions (total = 20 samples) are measured for hardness testing by Rockwell hardness testing method, as defined in ASTM E-18. The mean hardness value is defined by averaged value from five different areas on each specimen. This is measurement used ball indenter with a diameter 1/4 inch and Rockwell scale was HRB.

3.5.2 Tensile test

Five sintered tensile test bar specimens were used for each condition and a total of five conditions (total = 20 samples) were tested by Universal testing machine, Instron 8801 (according to ASTM E-8). The test process involves placing the test specimen and slowly extending and eventually fractures occur.

3.5.3 Surface preparation

The surface of all specimens was prepared by grinding on silicon carbide paper from mesh of 80# to 4000# and then polished with diamond suspend 6, 3, 1 μm. Then etch the polished surface by 2% Nital solution and use ethanol to clean the surface before the analyzation.

3.6 Wear test

Dry sliding wear experiments were carried out on ball-on-disc wear machine in accordance with ASTM G99-05(2010) and set up as Figure 3.27. The sliding velocity is 0.1 m/s at normal load 5N, 10N and 15N. All specimens were tested under sliding distance of 1,000 m at room temperature with relative humidity 60%. The specimen for tribometer test is disk specimens with roughness of 4-5 μm under a ball made of SKF chromium steel grade G20 that has diameter of 6 mm with hardness of 838 ± 21 HV and has roughness of 4 μm as a counterpart material. The friction coefficient graph was recorded from the measured of friction torque by using a load cell. The average mass loss was obtained from the mass of specimens' measurement before and after wear test. The volume loss of disk specimens was calculated as Equation 3.1., where R defined as wear track radius, and d defined as wear track width. The volume loss of a spherical ended pins was calculated as Equation 3.2., where d defined as wear scar diameter, and r defined as pin end radius. At the end of each test, the wear rate was calculated according to Equation 3.3. Worn surfaces and wear debris were investigated using a Scanning Electron Microscope to better understand the effect of processing on wear behavior and the wear mechanism.

$$\text{Disk volume loss} = 2\pi R\,[r2\sin\text{-}1(d/2r) - (d/4)(4r2\text{-}d2)1/2] \tag{3.1}$$

$$\text{Pin volume loss} = (\pi h/6)[3d2/4 + h2] \tag{3.2}$$

$$\text{Wear rate} = (\text{volume loss}/\text{distance}) \tag{3.3}$$

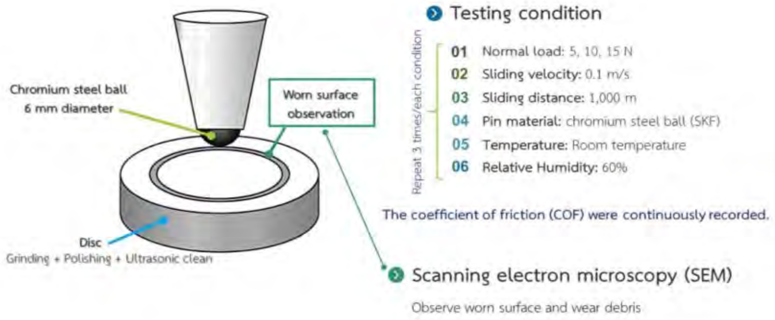

Figure 3-27 The schematic of ball-on-disc wear test set up

3.6.1 Microstructure Analysis

Optical Microscopy and Scanning Electron Microscopy are equipment to observe the microstructure of specimens. Optical microscopy is a common method for general inspection purposes but scanning electron microscopy can provide more surface and compositional detailed. Thus, this thesis used Optical Microscopy for analyst the overview of microstructure and use Scanning Electron Microscopy for analyst the details of microstructure.

3.6.2 X-Ray Diffraction Analysis

X-Ray Diffraction Analysis (XRD) is equipment used to Identify crystalline phases and orientation present in a material. All specimens for XRD were prepared by cutting, grinding, and polishing and performed by PANalytical X'pert pro with copper source (wavelength of 1.5406 Å) and conditions including step size of 0.2°, time of 0.5 s/step and angle of 30-110°.

CHAPTER 4

RESULTS AND DISCUSSION

4.1 Microstructure

4.1.1 General microstructure characterization by using OM and SEM

It was observed that the microstructural characters shown in Fig. 4.1 resemble austempered ductile iron with ausferrite matrix [37], ausferritic ductile cast iron [38], and those of sintered composites in [22, 39, 40]. It was found that a special microstructural feature called 'ausferrite' which consists of bainitic ferrite and austenite coexisted with ferrite and pearlite in Fe-Mo-Mn-Si-C sintered alloys with Mo ≥ 0.85 wt. %. The formation of austempered ductile iron-like microstructure was explained in [6]. An austempered ductile iron with an ausferrite (bainitic ferritic + austenite) microstructure is commonly obtained by a heat treatment called 'austempering' of an as-cast ductile iron [41]. The conditions under which ferrite and pearlite transformations occur in ductile irons are also briefly explained in [19].

In this work, the optical micrographs of the etched surface of Fe-1.5Mo-0.15Mn-4wt%SiC-varied Ni sintered composite materials, all samples demonstrate general microstructural features resembling of black particles enveloped with ferrite halos, pearlite nodules, and ausferrite as illustrated in Figure 4.1. The black particles which contain graphite had different shapes from spherical to irregular shapes. The sizes of black particle shapes also varied from a small to 100 microns. On the other hand, the white-colored ferrite halos around black particles contained ferrite grains. The optical micrograph of sintered composite 00Ni showed microstructural features consisting of black particles enveloped with ferrite halos, pearlite nodules, and ausferrite (Figure 4.1a). The sintered 05Ni composite showed microstructural features (Figure 4.1b) similar to that of the sintered 00Ni composite (Figure 4.1a), except that the ausferrite fraction was increased whereas the pearlite fraction was slightly decreased. The total area of each phase in microstructural components of all sintered composite materials was measured and presented in Table 4.1. The ausferrite structure could be clearly observed in the SEM images as shown in Figure 4.2. The pearlite fraction in sintered 10Ni composite decreased significantly while the ausferrite fraction was the predominant microstructural component (Figure 4.1c). The ausferrite structure could be clearly observed in the SEM image (Figure 4.2c). The pearlite nearly disappeared from sintered 15Ni (Figure 4.1d) and 20Ni (Figure 4.1e) composites while the ausferrite fraction became the predominant microstructural component in 15Ni and 20Ni sintered composites. According to the experimental results, it was found that the ausferrite fraction increases as the nickel content increases. That is why it may be concluded that in Ni-added sintered composites of Fe-1.5Mo-0.15Mn-4wt.%SiC-(0.5-2wt.%Ni), Nickel has a strong promoting influence on the development of ausferrite formation.

Table 4-1 Total area of each phase of sintered materials

Sintered Composites	Area Fraction (%)			
	Black particle	Ferrite Halos	Pearlite	Ausferrite
00Ni	15.6	23.9	28.2	32.3
05Ni	8.9	14.8	25.5	50.8
10Ni	7.7	7.3	20.4	64.6
15Ni	3.8	2.6	12.9	80.7
20Ni	2.7	1.2	11.6	84.5

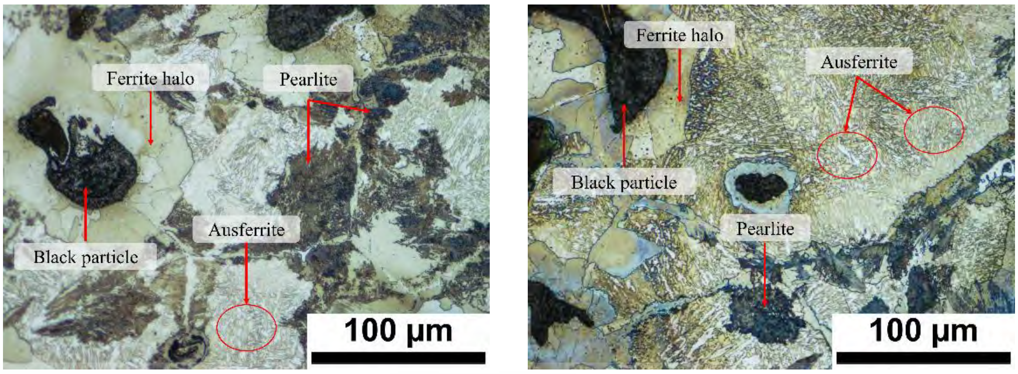

(a) 00Ni sintered composite (b) 05Ni sintered composite

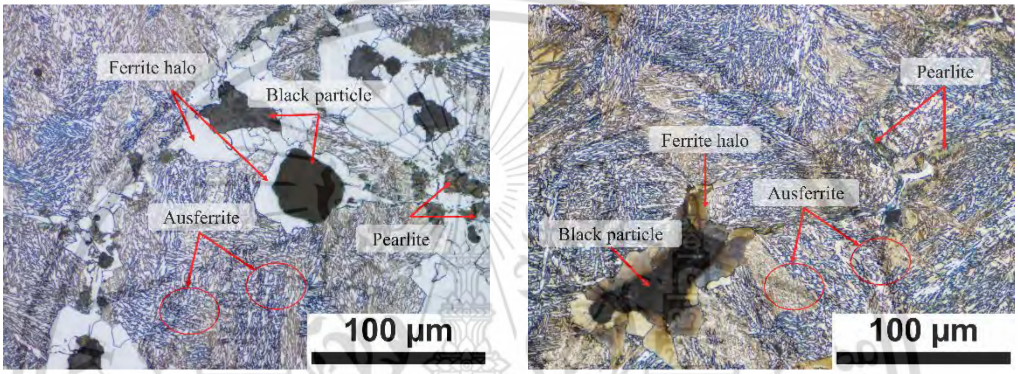

(c) 10Ni sintered composite (d) 15Ni sintered composite

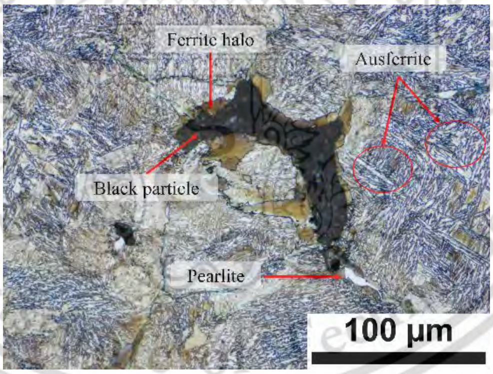

(e) 20Ni sintered composite

Figure 4-1 Optical micrographs of Fe-Mo-Mn-Si-C-Ni sintered composite

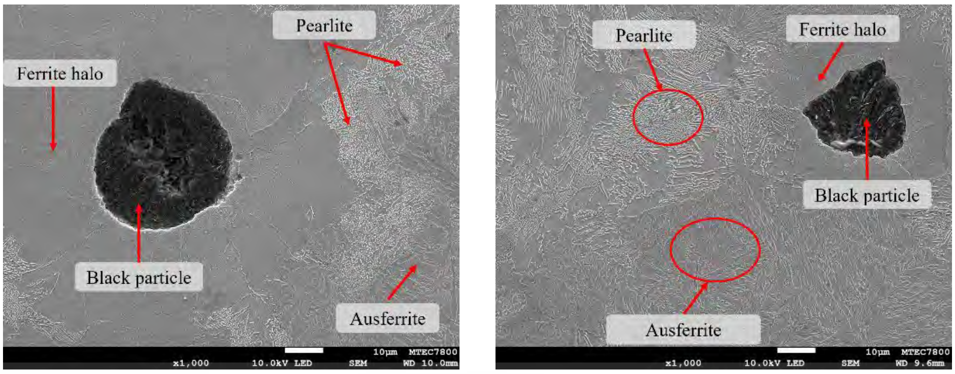

(a) 00Ni sintered composite (b) 05Ni sintered composite

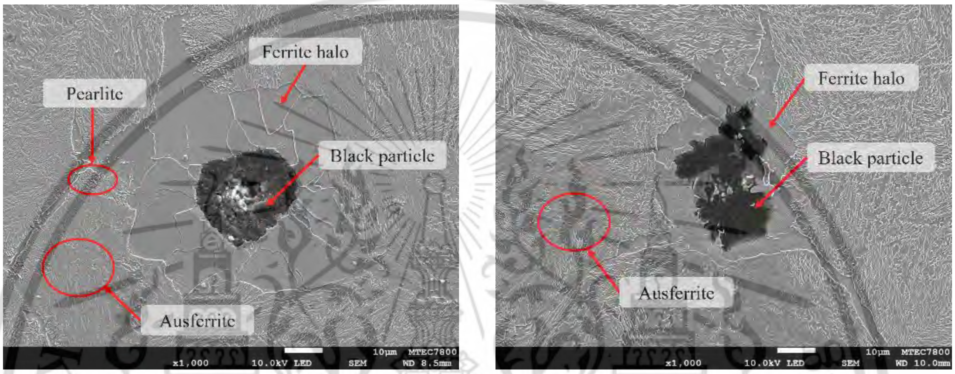

(c) 10Ni sintered composite (d) 15Ni sintered composite

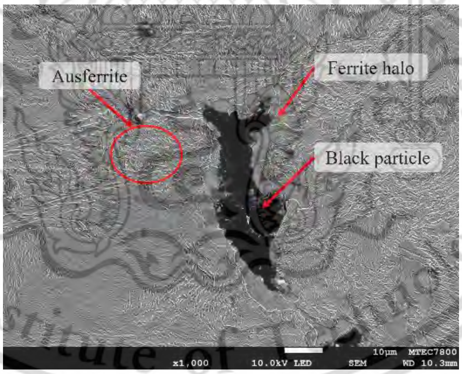

(e) 20Ni sintered composite

Figure 4-2 SEM micrographs of Fe-Mo-Mn-Si-C-Ni sintered composites

4.1.2 Sintered 00Ni composite

The sintered composite 00Ni (Figure 4.3a) showed general microstructural features mostly found in austempered ductile iron, consisting of black particles enveloped with ferrite halos, pearlite nodules, and ausferrite. To further validate the matrix components, a two-stage tinting method was applied to the 00Ni sintered composite. A colored OM image showed a black particle surrounded by a white-colored halo, which was identified as ferrite. Dark-colored areas were identified by SEM as lamellar pearlite structure (Figure 4.3c), and ausferrite was identified as a bright white and light blue colored region (Figure 4.3b). The plates of ferrite, pearlite nodules, bainitic ferrite, and austenite can be clearly observed in SEM images (Figure 4.3c-d). From SEM images, it can be confirmed that 00Ni sintered composite exhibits ausferrite mictostructure that contains bainitic ferrite plates + austenite plates. Strong peaks of α-ferrite (bcc crystal structure), weak peaks of γ-austenite (fcc crystal structure), and carbide $(\mathrm{Fe_3C})$, orthorhombic crystal structures were observed in the XRD pattern (Figure 4.3e) of the 00Ni sintered composite.

According to the SEM image (Figure 4.3d), 00Ni sintered composite is also composed of a mixture of coarse bainitic ferrite and austenite resembling that of an upper ausferrite which typically form at higher austempering temperatures [42-43]. That is why it can be confirmed that the microstructure of 00Ni sintered composite is comprised of black particles, ferrite halos, pearlite nodules, and upper ausferrite. Surprisingly, it was found that 00Ni sintered composite has microstructural characteristics that are similar to those of an ausferritic (austempered) ductile cast iron (ADCI) [19, 22, 37–40] which has different portions of ferrite, carbides $(\mathrm{M_3C})$, upper bainite, and ausferrite. Due to the slow cooling process in the furnace during the production of the 00Ni composite through sintering, the emergence of upper ausferrite within its matrix signifies the substantial impact of the composite's chemical composition on the promotion of bainitic ferrite and the stabilization of γ-austenite.

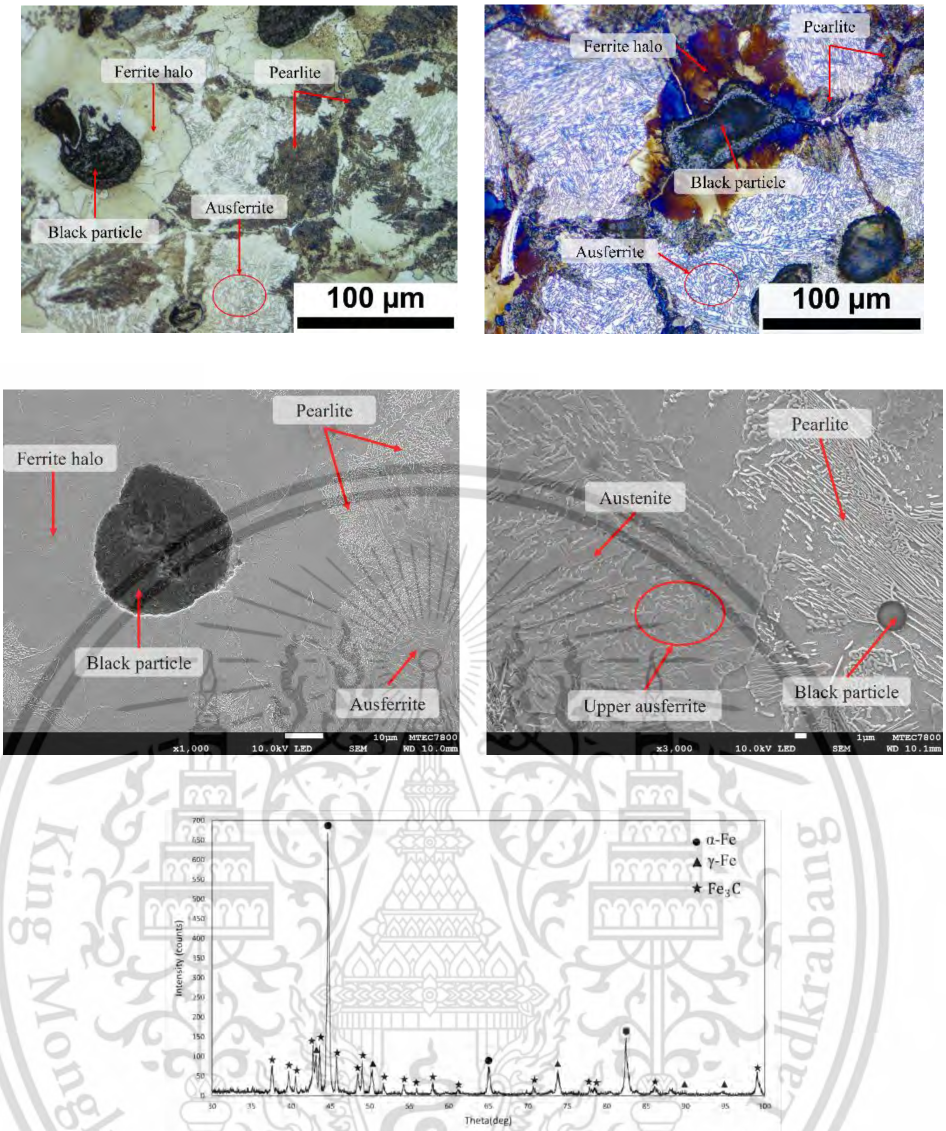

Figure 4-3 Investigation on microstructure of 00Ni sintered composite; (a) Optical micrograph image showing basic microstructural features, (b) Color OM image showing pearlite and upper ausferrite, (c) SEM image showing general microstructural features (d) SEM image showing bainitic ferrite, austenite, and upper ausferrite, and (e) XRD patterns of microstructural components.

4.1.3 Sintered 05Ni composite

When 0.5wt% of Ni was used to produce 05Ni sintered composite, the ausferrite fraction was slightly increased while the black particles, pearlite nodules, and ferrite halos started to decrease (Figure 4.4a and Table 4.1). The matrix of 05Ni sintered composite is composed of similar microstructural features of ausferritic (austempered) ductile iron such as ferrite halo, black particle, pearlite, and upper ausferrite as shown in SEM image (Figure 4.4d). Strong peaks of γ-austenite (fcc), α-ferrite (bcc), and carbides (Fe_3C) overlap each other in the XRD pattern (Figure 4.4e) of the 05Ni sintered composite. Since Nickel addition resulted in a decrease of the black particle count and pearlite nodules and an increase of the upper ausferrite fraction (Table 4.1), it can be inferred that the addition of Ni 0.5wt.% promotes the formation of upper ausferrite which has higher bainitic ferrite plates and improved austenite stability (Figure 2d).

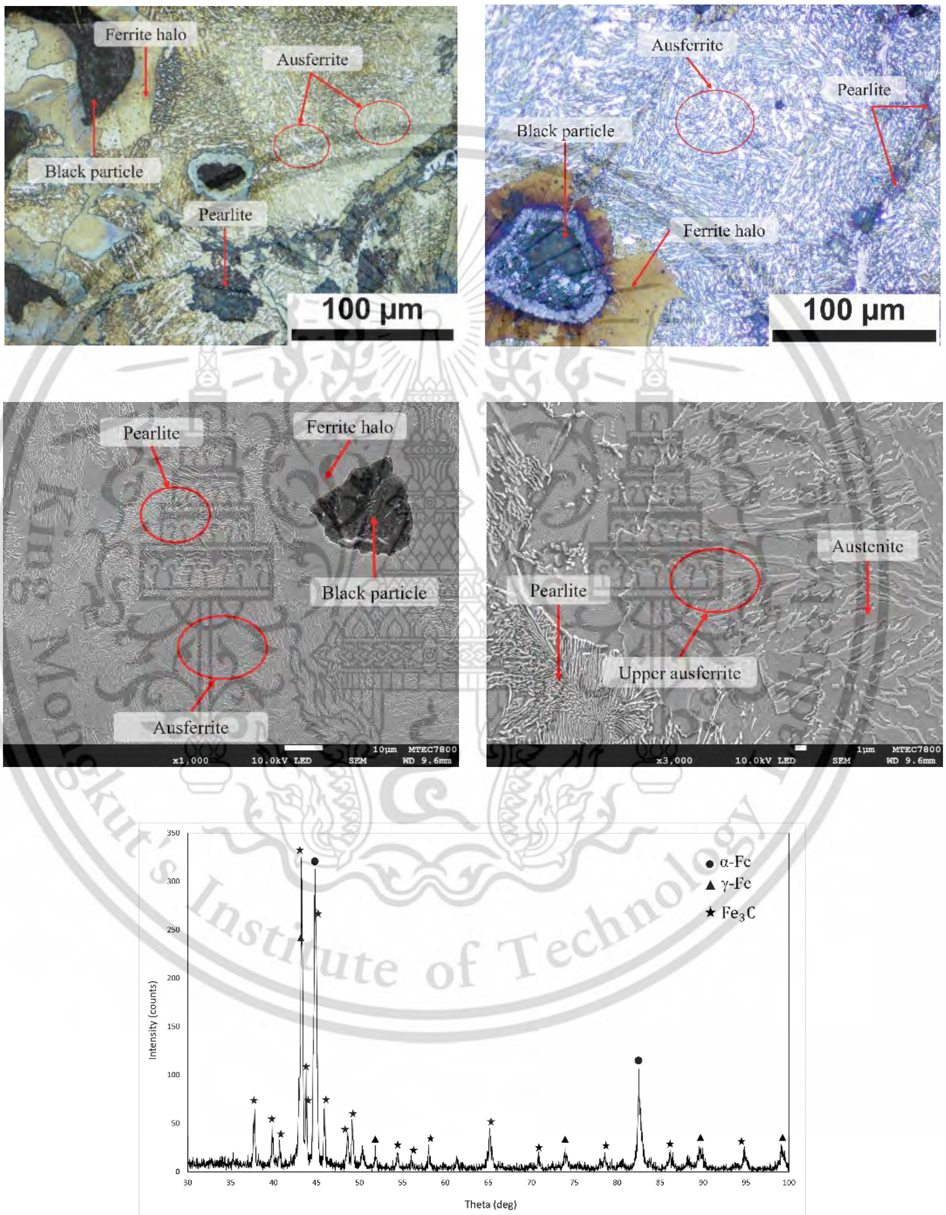

Figure 4-4 Investigation on microstructure of 05Ni sintered composite; (a) Optical micrograph image showing basic microstructural features, (b) Color optical micrograph image showing pearlite and upper ausferrite, (c) SEM image showing general microstructural features (d) SEM image showing bainitic ferrite, austenite and upper ausferrite, and (e) XRD patterns of microstructural components.

4.1.4 Sintered 10Ni composite

When 1.0wt% of Nickel powder was added to produce a sintered 10Ni composite, a black particle, ferrite halos, pearlite nodules, and upper ausferrite (Figure 4.5a) summed up the microstructural features of 10Ni sintered composite. A slight change in the morphology of ferrite halos, and a decrease in the percentage of black particle and pearlite counts (Figure 4.5 and Table 4.1) were among the notable microstructural changes. The pearlite fraction in sintered 10Ni composite decreased significantly while the ausferrite fraction was the predominant microstructural component. The SEM images revealed that the 10Ni sintered composite is still an upper ausferrite but there is a slight reduction in bainitic ferrite component thickness (Figure 4.5c and d) while most of the austenite component thickness remains unchanged. Mild peaks of α-ferrite (bcc), strong peaks of carbide $(\mathrm{Fe_3C})$ and γ-austenite (fcc) are observed in the XRD pattern (Figure 4.5e) of the 10Ni sintered composite.

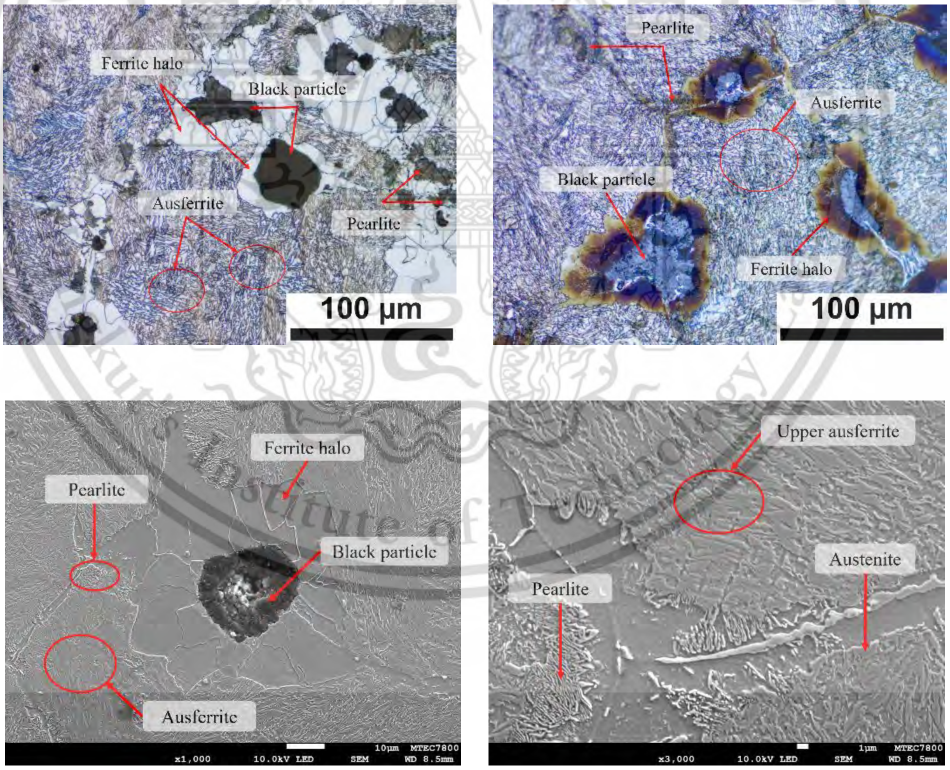

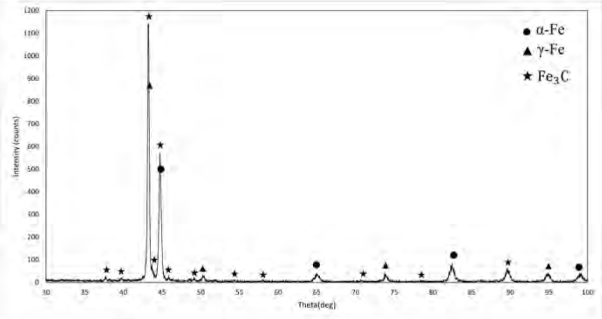

Figure 4-5 Investigation on microstructure of 10Ni sintered composite; (a) Optical micrograph image showing basic microstructural features, (b) Color OM image showing pearlite and upper ausferrite, (c) SEM image showing general microstructural features (d) SEM image showing bainitic ferrite, austenite, and upper ausferrite, and (e) XRD patterns of microstructural components.

4.1.5 Sintered 15Ni composite

When 1.5wt% of Nickel powder was used to produce 15Ni sintered composite, black particles, ferrite halos, pearlite nodules, and ausferrite (Figure 4.6a). (Figure 4.6a) summed up the microstructural features of 15Ni sintered composite. A significant change in the morphology of ferrite halos, a significant decrease in black particle count, and pearlite nodules (Figure 4.6 and Table 4.1) are among the notable microstructural changes. The pearlite nodules and ferrite halos nearly disappeared while the ausferrite fraction became the predominant microstructural component in sintered 15Ni (Figure 4.6d). A partial deposit of ferrite grains on a black particle surface served as proof of the ferrite halo degradation. The thickness of the austenite and bainitic ferrite components were both decreased, according to the SEM pictures (Figure 4.6c-d). The presence of a lower ausferrite which can provide improved toughness and ductility is clearly visible under high-magnification SEM images. According to the SEM image, it was observed that the lower ausferrite is composed of austenite and fine bainitic ferrite [44-45]. That is why it can be confirmed that the matrix of sintered 15Ni composite is comprised of a decreased fraction of black particles, ferrite halos, and pearlite nodules while most of the region of the matrix was occupied by lower ausferrite. Mild peaks of γ-austenite (fcc), strong peaks of carbide (Fe_3C) and α-ferrite (bcc) are observed in the XRD pattern of 15Ni sintered composite (Figure 4.6e). Given that the lower ausferrite is generally known to occur at a lower temperature than the upper ausferrite, it can be inferred that the addition of 1.5wt.% Nickel expands the transformation temperature range of bainitic ferrite while increasing the stability of austenite.

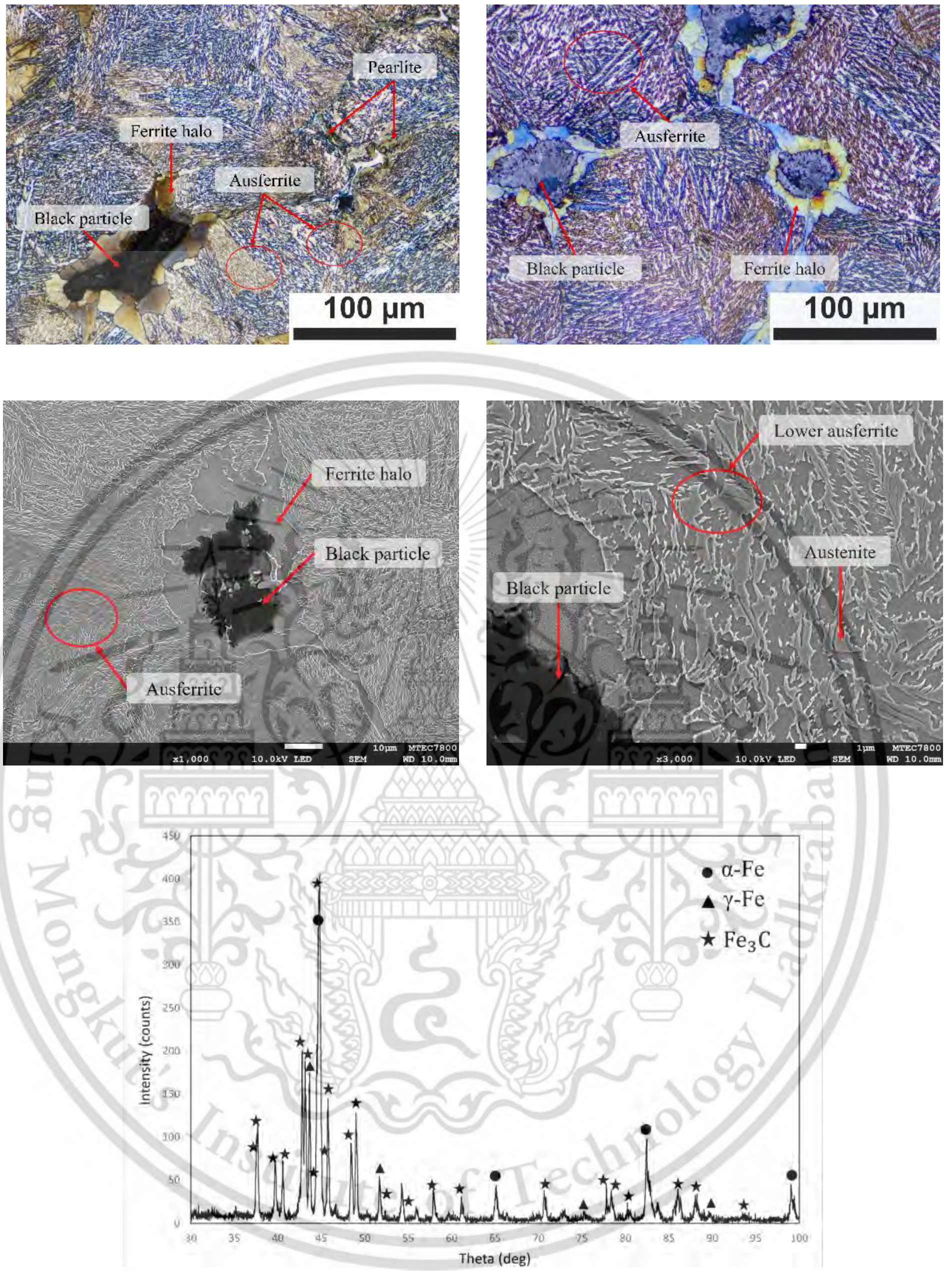

Figure 4-6 Investigation on microstructure of 15Ni sintered composite; (a) Optical micrograph image showing basic microstructural features, (b) Color OM image showing pearlite and ausferrite, (c) SEM image showing general microstructural features (d) SEM image showing bainitic ferrite, austenite, and lower ausferrite, and (e) XRD patterns of microstructural components.

4.1.6 Sintered 20Ni composite

When 2.0wt% of Nickel powder was used to produce 20Ni sintered composite, black particles, ferrite halos, pearlite nodules and ausferrite (Figure 4.7a) summed up the microstructural features of 20Ni sintered composite. The ferrite halo and pearlite nearly disappeared while the ausferrite fraction became the predominant microstructural component occupying the overall matrix in 20Ni sintered composite (Figure 4.6d). The SEM images revealed low bainitic ferrite (acicular needle-like) and austenite laths (Figure 4.7c-d) which indicates the increased fraction of lower ausferrite formation. That is why it can be confirmed that the matrix of sintered 20Ni composite is comprised of a decreased fraction of black particles, ferrite halos, and pearlite nodules while most of the region of the matrix was occupied by the increased fraction of lower ausferrite (Figure 4.7 and Table 4.1). Strong peaks of γ-austenite (fcc), mild peaks of α-ferrite (bcc), and significantly low peaks of carbide (Fe_3C) were observed in the XRD pattern of 20Ni sintered composite (Figure 4.7e).

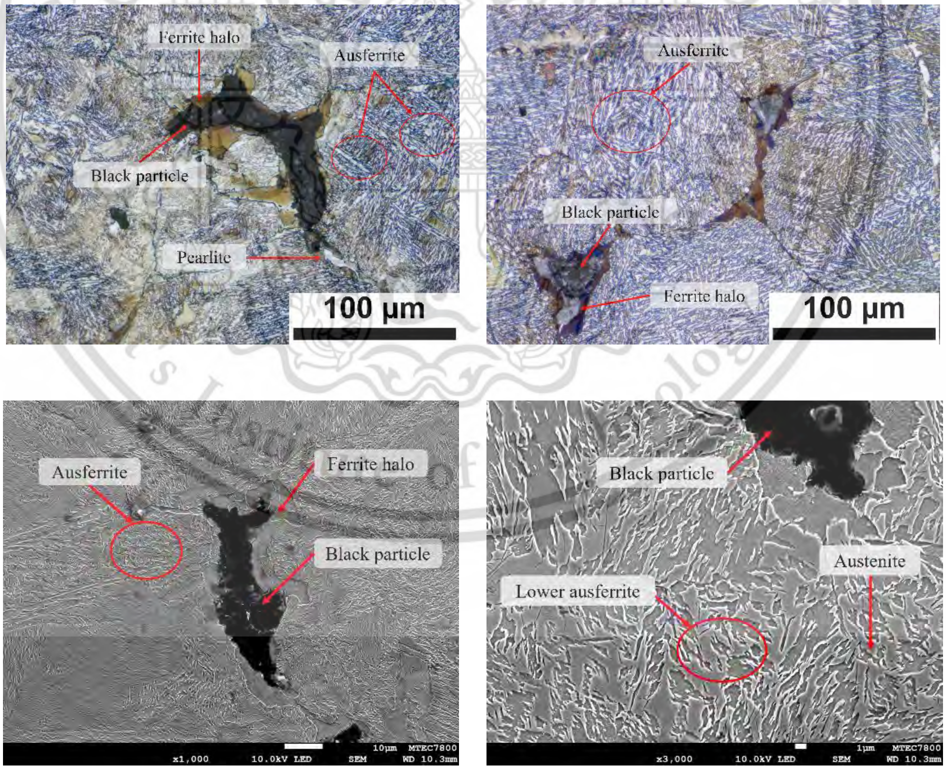

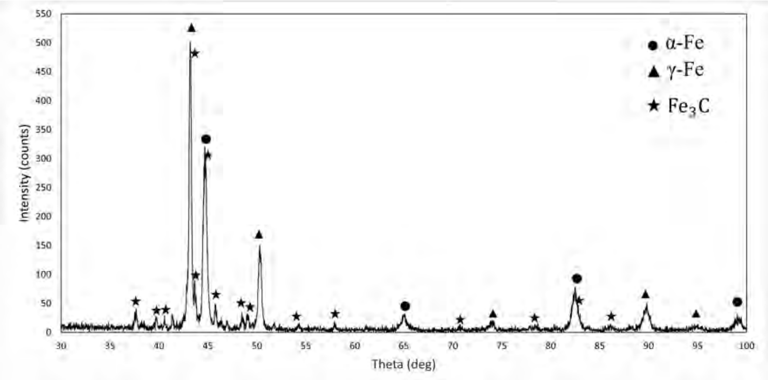

Figure 4-7 Investigation on microstructure of 20Ni sintered composite; (a) Optical micrograph image showing basic microstructural features, (b) Color OM image showing pearlite and ausferrite, (c) SEM image showing general microstructural features (d) SEM image showing bainitic ferrite, austenite, and lower ausferrite, and (e) XRD patterns of microstructural components.

4.2 The influence of Ni on black particles and ferrite halos

The elemental composition of a black particle, pearlite, ferrite, and ausferrite from EPMA analysis (Figure 4.8) can be used to derive the influence of Ni on the formation mechanism of black particles and ferrite halos in sintered composites. The black particle was made up of a solid core and a graphite nodule (Figure 4.8a). The concentration of carbon is extremely high in the graphite nodules of the black particle while comparatively high C concentrations were found in the austenite plates of ausferrite and the solid core of the black particle (Figure 4.8b). The Si elements are evenly dispersed through the matrix and comparatively higher concentrations in the solid core of the black particle (Figure 4.8c). The Ni, Mn, Mo, and Fe elements are also evenly dispersed in the matrix (Figure 4.8d, 4.8e, 4.8f, and 4.8g).

The chemical reaction between Fe-1.5Mo and SiC powder particles during heating and sintering holding results in local melting around the peripheries of prior SiC particle sites resulting in SiC decomposition by generating Si and C atoms [44–46]. Si and C atoms diffuse into the austenite Fe-1.5Mo matrix and then act as nuclei for the reprecipitation of graphite to form the black particle on the solid core surface during continuous cooling. The formation of ferrite grain is presented around the nodule because of the **α**-iron or ferrite phase stability around the SiC particles which in turn leads to the diffusion of dissolved C atoms back to the black particles as illustrated in Figure 4.8b [22], [39]. At a distance far away from the black particles, the dissolved carbon atoms also precipitate as cementite $(\mathbf{Fe_3C})$ in pearlite structure [43, 47–49]. The atoms of Ni powder melt and diffuse into the Fe-1.5Mo matrix undergoing favored suppression of black particles and ferrite halos.

The experimental results, shown in Figs. 4.3, 4.4, 4.5, 4.6, and 4.7 reveal how black particles and ferrite halos alter as the Ni content increases. Table 2 demonstrates the analytical results of black particle and ferrite halo count determined by the ImageJ program. The black particle count was reduced when Ni was introduced to Fe-1.5Mo-Mn-Si-C. The decrease in black particle count caused by Ni addition in sintered composites opposes the increase of black particle count which contains graphite in ductile cast irons [50]. This is because Ni and SiC melt completely and Ni segregates negatively around the graphite nodules resulting in population reduction of the solid core and black particles [51]. The thickness of the ferrite halo correspondingly diminishes as the Ni concentration increases. From the experimental results, the ferrite halo thickness around the black particle nearly disappears in Fe-Mo-Mn-Si-C-Ni composite with Ni ≥1.5wt.%. This is due to the influence of Ni in lowering the driving force associated with ferrite/austenite formation. It was found in Figure 8 of reference [19] that any addition of Ni, Cu, and Mn at a given temperature lowers the driving force (∆WC) for C diffusion from austenite to graphite and hence reduces the formation of ferrite halos.

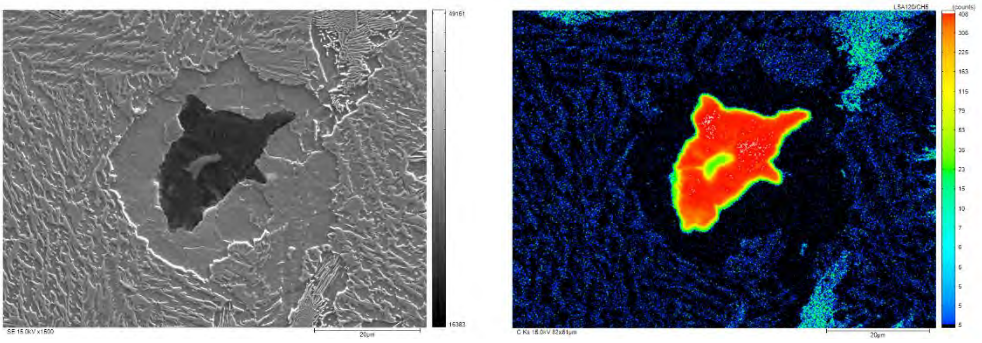

Carbon

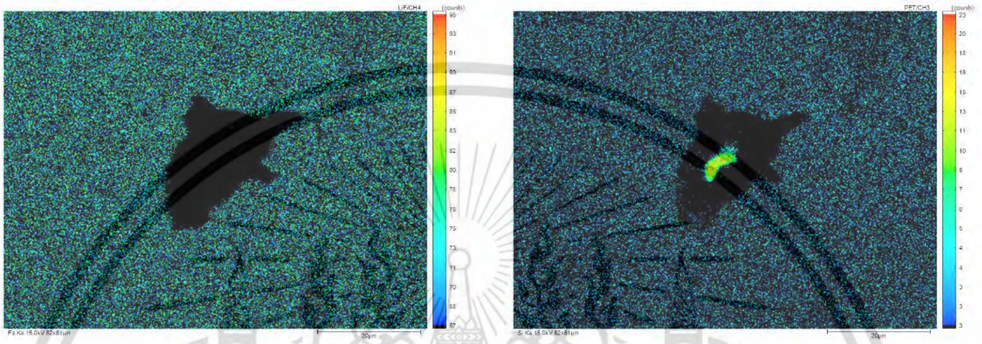

Iron

Silicon

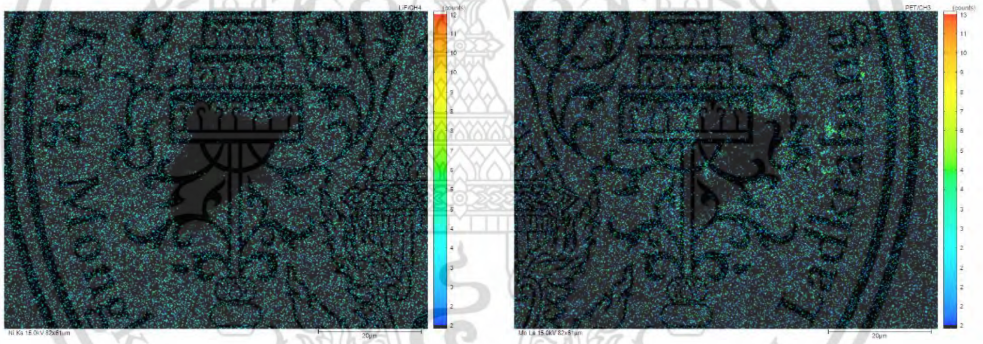

Nickel

Molybdenum

Manganese

Figure 4-8 Electron probe microanalysis of sintered composites (a) SEM image of 20Ni, (b) C, (c) Si, (d) Ni, (e) Mn, (f) Mo, and (g) Fe.

4.2.1 The influence of Ni on ausferrite fraction and component thickness

According to the experimental results as shown in Fig 4.1 and Table 4.1, it was found that the ausferrite fraction increases as the Ni content increases in Fe-Mo-Mn-Si-C-Ni sintered composites. The ausferrite fraction is highest in the sintered 15Ni and 20Ni sintered composite. There was some report on the effect of Ni addition in ADI that the addition of Ni leads to an increased percentage of ausferrite formation. This is due to the properties of Ni which was known as an austenite stabilizing element and the lesser activation energy requirement to induce the ausferrite transformation reaction [52]. As more and more Ni was added, it was found that the ausferrite component thickness was reduced gradually. The sintered 00Ni, 05Ni, and 10Ni show the formation of upper ausferrite which has coarser acicular ferrite and high carbon stabilized austenite. The sintered 15Ni and 20Ni composite show the formation of lower ausferrite which consists of thickness reduced fine acicular bainitic ferrite. The reduction of ausferrite component thickness is commonly attributed to ausferrite transformation temperature. It was found that the lower the austempering temperature the finer the ausferrite scale in ADI [43-53]. That is why it can be concluded that the reduction of ausferrite component thickness in sintered Ni-added composite implies that Ni lowers the transformation temperature of ausferrite which leads to more formation of lower ausferrite (fine acicular bainitic ferrite + austenite).

4.3 Mechanical properties

The experimental sintered composites showed high hardness values of 101-106 HRB (Figure 4.9a), high ultimate tensile strengths of 800-1200 MPa (Figure 4.9b), and high yield strengths of 400-600 MPa (Figure 4.9c). While the values of elongation at break were in the range of 2.6-4.9% (Figure 4.9d). The tensile properties and hardness of sintered composites depended strongly on microstructural components, such as black particles, ferrite halos, pearlite, and ausferrite.

All sintered Ni-added composites demonstrate lower values of tensile strength and hardness, however 10Ni sintered composite which consists of ferrite-pearlite-upper ausferrite microstructure demonstrates the highest tensile strength and hardness among others. This evidence indicates that an increase of Ni content up to 1.0wt% results in increased hardness and tensile strength while Ni content of 1.5 and 2.0wt%

sintered composite results in decreased hardness and tensile strength. These results may be attributed to upper ausferrite to lower ausferrite transformation along with the degeneration of ferrite and pearlite as revealed by SEM in Figure 4.2 and Table 2. This combined effect leads to the increase of hardness and tensile strength in Ni-added sintered composite of up to 1.0 wt.%. The reduced hardness and tensile strength in 15Ni and 20Ni sintered alloys were probably due to the presence of lower ausferrite and high-volume fraction of austenite as indicated in Table 2 and Figure 4.6-4.7.

The elongation values were unsystematically related to tensile strengths. All Ni-added sintered composites displayed lower values of elongation, but 20Ni sintered composite with lower ausferrite matrix displayed the highest elongation value (Figure 4.9d). This evidence indicates that an increase of Ni content up to 2.0wt% enabled to production of more formation of lower ausferrite which leads to the increased percentage of elongation in Ni-added composites.

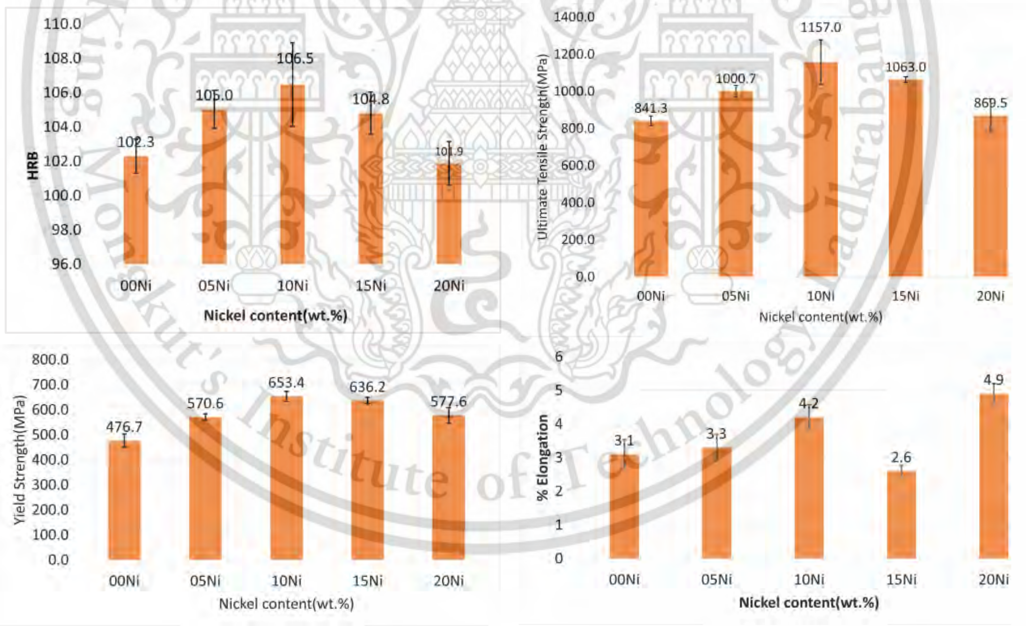

Figure 4-9 Mechanical characteristics of Fe-Mo-Mn-Si-C-(Ni) sintered composites; (a) Ultimate tensile strength, (b) Yield strength, (c) Elongation, and (d) Macro-hardness.

4.4 Friction coefficient

The friction coefficient of Fe-Mo-Mn-Si-C-Ni sintered alloys were examined at various conditions. The specimens were tested at normal loads 5N, 10N, and 15N with a sliding velocity of 0.1 m/s. All specimens were tested under sliding distance of 1,000 m at room temperature with 60% relative humidity. The specimen for the tribometer test is a disk specimen with a roughness of 4-5 µm under a ball made of SKF chromium steel grade G20 that has a diameter of 7mm with a hardness of 838 ± 21 HV and has roughness of 4 µm as a counterpart material.

The influence of different Ni contents on the friction coefficient of all sintered composites at normal loads 5N, 10N, and 15N are shown in Figure 4.10-4.12. All sintered composites generally show the two stages of the wear mechanism, the run-in stage, and the stable stage. The run-in stage is shown at the first period of the graph about 0-100m which demonstrates the unsteady friction coefficient because of the low roughness of the point contact between the ball and sintered composite surface at the initial distance. On the other hand, after the test ran into a higher distance of more than about 100m, the friction coefficient became a steady state with increasing friction distance. The friction coefficient at steady state of sintered all composites is decreased from the run-in state because the friction between the counter ball and the sintered composites changes from point contact to surface contact, and the graphite particles are flake off from the surface and lubricate leading to the decreasing of the friction coefficient [54]. Furthermore, these results show that the friction coefficient increases with increasing normal load, which is due to an increase in adhesion strength. This is because, at low normal loads, the oxide film efficiently separates two metal contact surfaces, resulting in less metallic contact and a low friction coefficient. While under increased normal load, the oxide film broke down, resulting in intimate metallic contact and an increase in adhesion strength, leading in a higher friction coefficient [55].

It was observed that the friction coefficient of Fe-Mo-Mn-Si-C composite, 00Ni has an overall lower coefficient of friction than all the other Ni-added sintered composites as shown in Table 4.2 below. This is attributed to an increased fraction of black particles which contain graphite nodules and silicon core which act as a solid lubricant on the material surface, it reduces the direct contact area between two surfaces, which results in a decrease of the friction coefficient. The coefficient of friction in Ni-added sintered composites 05Ni, 10Ni, and 15Ni was increased due to the reduced formation of graphite nodules in these sintered composites. However, 20Ni sintered composite has a relatively equal and lower coefficient in contrast with 00Ni. This can be attributed to more formation of lower ausferrite fractions in 20Ni sintered composite which provides higher friction resistance [42].

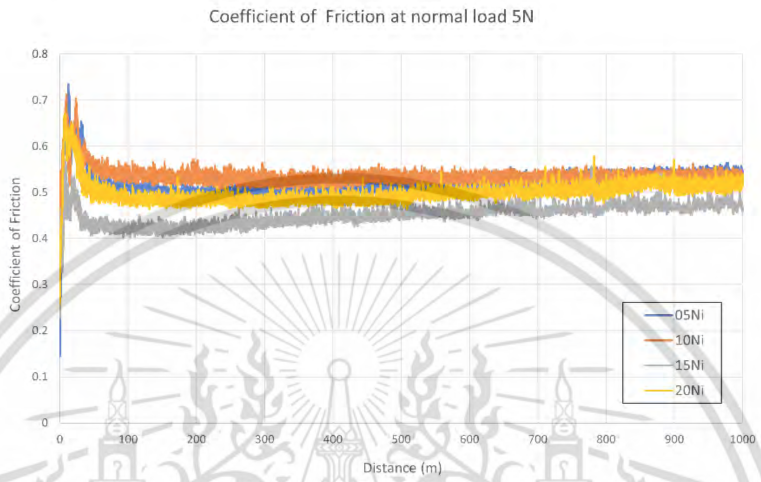

Figure 4-10 The friction coefficient at load 5N of all sintered composites

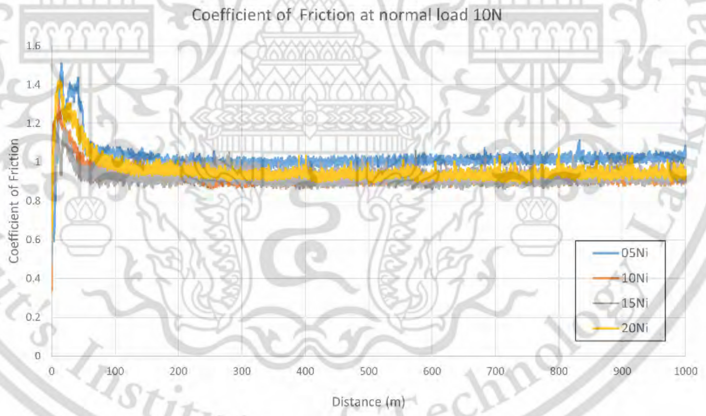

Figure 4-11 The friction coefficient at load 10N of all sintered composites

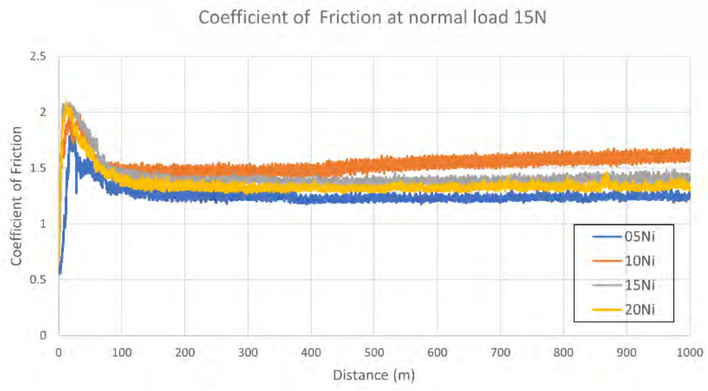

Figure 4-12 The friction coefficient at load 15N of all sintered composites

Table 4-2 Coefficient of friction of all sintered composites with varied Nickel content

Varied Ni Content	Coefficient of Friction		
	5N	10N	15N
00Ni	0.4412	0.4402	0.5099
05Ni	0.5205	0.5129	0.4191
10Ni	0.5365	0.4634	0.5148
15Ni	0.4508	0.4648	0.4747
20Ni	0.4993	0.4800	0.4539

4.5 Wear rates

The wear rate corresponding to sliding distance and normal applied load which are used to express the material removal during the tribology test are listed in Table 4.3. The effect of different normal applied loads 5N, 10N, and 15N on the wear rate of Fe-Mo-Mn-Si-C-Ni sintered alloys at a constant sliding speed of 0.1 m/s is shown in Figure 4.13. It is inferred that the wear rate of all sintered composite is proportional to the normal load, the more increase in normal load, the more the wear rate increases. This phenomenon occurs when an increase in normal load leads to the thermal softening of the material, and crack propagation results in the easier formation of wear fragments.

It was observed that 00Ni and 20Ni sintered composite has the lowest optimal wear rate and 10Ni have the highest wear rate as shown in Table 4.3 and Figure 4.13. The following are possible reasons for this behavior. The increasing wear rate of Ni-added sintered composites 05Ni, 10Ni, and 15Ni is due to the decreased count of graphite nodules which act as solid lubricant on the surface, and higher percentage of upper ausferrite in the matrix which is known to provide higher hardness that impacted to the sintered composites related with Archard's law which inferred that wear resistance is proportional to hardness [56]. However, 20Ni sintered composite has a relatively equal and lower wear rate in contrast with 00Ni. This can be attributed to the more formation of lower ausferrite fractions in 20Ni sintered composite which provides higher wear resistance than upper ausferrite [57].

Table 4-3 Wear rate of Fe-Mo-Mn-Si-C-(Ni) sintered alloys under different Nickel content.

Sintered composite	Wear Rate at specific normal load (N/mm^3)		
	5N	10N	15N
00Ni	3.92	7.70	10.78
05Ni	6.16	9.36	16.1
10Ni	4.84	10.7	21.6
15Ni	4.48	12.7	16.1
20Ni	5.48	9.84	11.9

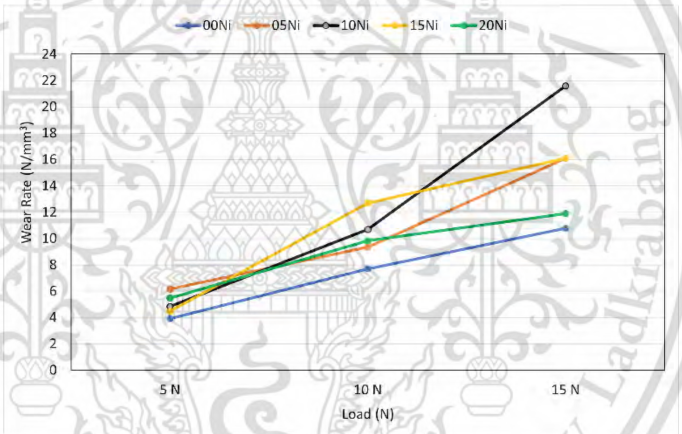

Figure 4-13 Wear rate at load 5N, 10N and 15N of Fe-Mo-Mn-Si-C-(Ni) sintered composites.

4.6 Worn surfaces and wear debris

4.6.1 Worn surfaces of all sintered composite at normal load 15N

The SEM micrographs of the worn surface of Fe-Mo-Mn-Si-C-(Ni) sintered alloys were compared under normal load 15N, which is shown in Figure 4.14. The typical wear mechanism in all sintered composites in this work is adhesive wear, delamination wear and abrasive wear as shown in the SEM image. Abrasion wear is induced by sliding against a hard surface when under normal load, which results in plastic deformation and scratching on the surface as abrasive grooves parallel to the sliding direction [57-58]. The delamination craters that occurred from the thermal softening of the surface were elongated along the sliding direction. Furthermore, the worn surface of all sintered composites illustrates the oxide agglomerates which is referred to as oxidative wear [57]. The results from the worn surface micrographs indicated an increase in Ni content increased the degree of surface damage and delamination wear which acts as a dominant wear mechanism in all sintered composites. This is because the specimen's coefficient of friction increases with increasing Ni content, which might lead to an increase in shear pressures applied to the material's sub-surface layer during sliding. Higher shear stresses increase the presence of nucleation and growth of the subsurface fracture, as well as the symptoms of the delamination mechanism. As a result of the material's lower resistance to crack propagation, the volume loss and wear rate increase with increasing Ni content.

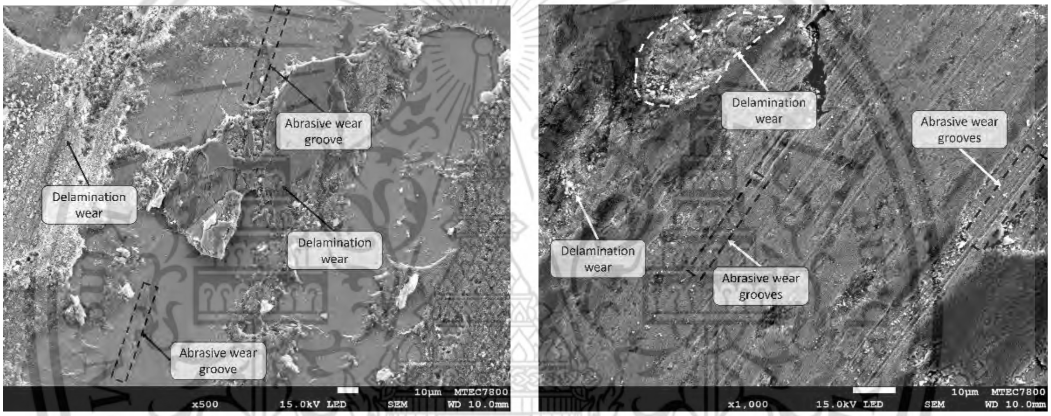

(a) 05Ni sintered composite (b) 10Ni sintered composite

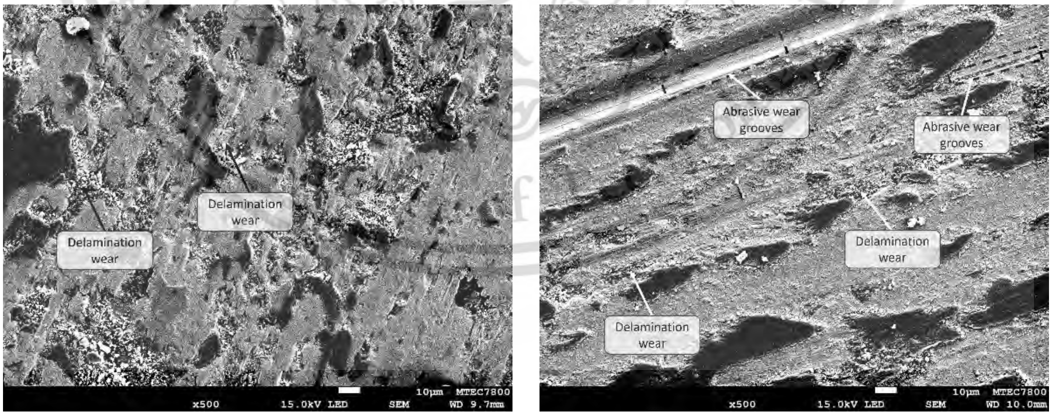

(c) 15Ni sintered composite (d) 20Ni sintered composite

Figure 4-14 SEM micrograph of worn surface of all sintered composites at load 15N

4.6.2 Worn debris of all sintered composite at normal load 15N

The SEM micrographs of wear debris of Fe-Mo-Mn-Si-C-Ni sintered alloys were compared after the wear test at normal load 15N, which is shown in Figure 4.15. The wear debris of sintered composites was formed due to the severe plastic deformation showing irregular geometry which confirms the delamination wear mechanism. Whereas the debris formed at Nickel content 2wt.% was a large and plate-like structure which indicates the adhesion wear [58].

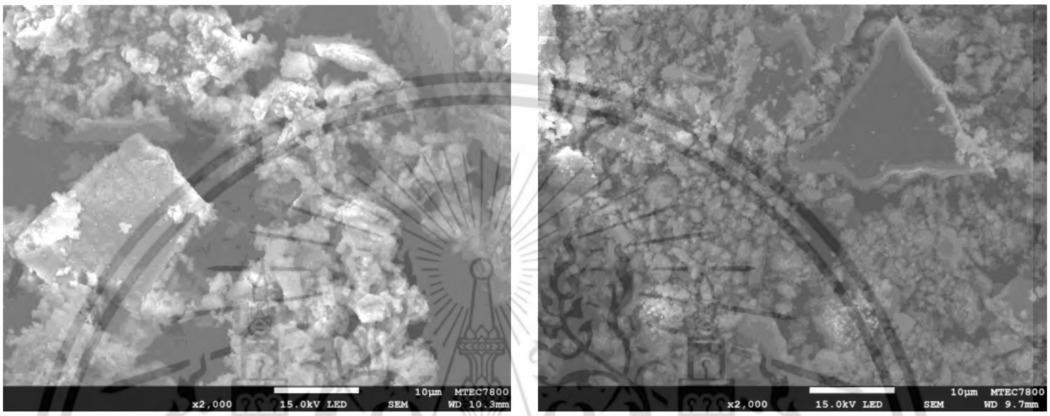

(a) 05Ni sintered composite (b) 10Ni sintered composite

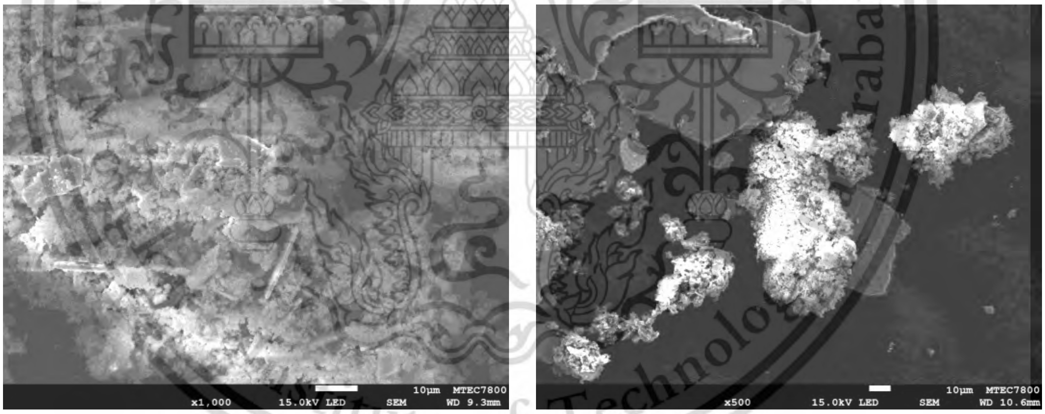

(c) 15Ni sintered composite (d) 20Ni sintered composite

Figure 4-15 SEM micrograph of wear debris of all sintered composites at load

4.6.3 Worn surfaces and wear debris of sintered 05Ni composite

The SEM micrographs of worn surfaces and wear debris at all normal load conditions of Fe-Mo-Mn-Si-C-Ni sintered alloys are shown in Figure 4.16 and 4.17 respectively. Delamination wear and adhesion wear are present on worn surfaces at all normal loads. The wear debris at 5N, 10N, and 15N show irregular geometry as the delamination wear, and a plate-like structure which also confirms the adhesion wear.

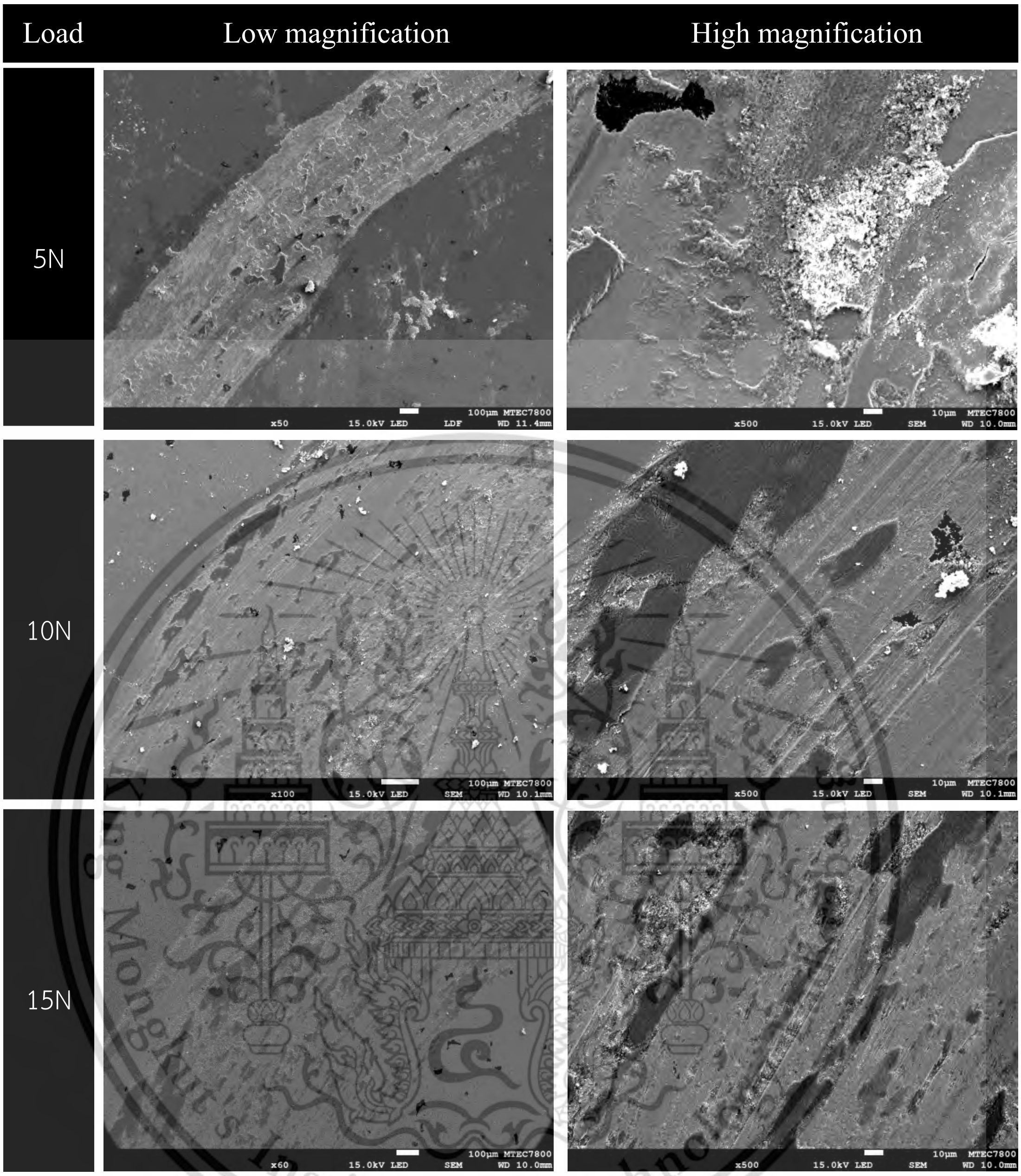

Figure 4-16 The SEM micrograph of the worn surface of sintered 05Ni composites

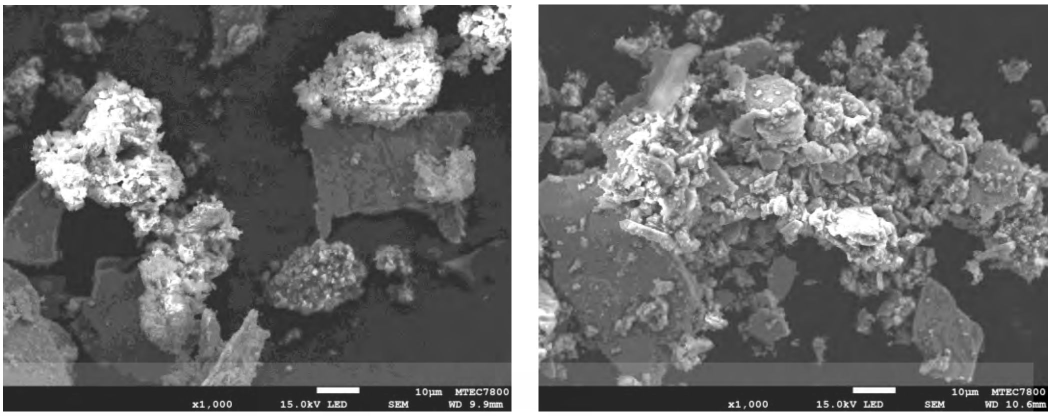

(a) Wear debris at load 5N
(b) Wear debris at 10N

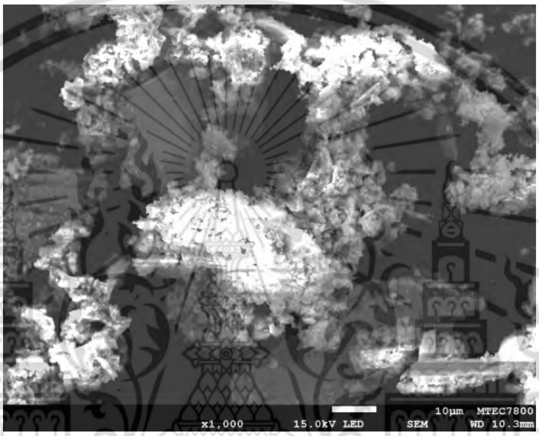

(c) Wear debris at load 15N

Figure 4-17 The SEM micrograph of wear debris of sintered 05Ni composite

4.6.4 Worn surfaces and wear debris of sintered 10Ni composite

The SEM micrographs of worn surfaces and wear debris at all normal load conditions of sintered 10Ni composite are shown in Figure 4.18 and 4.19 respectively. The mechanism of wear are abrasive wear grooves and delamination wear which confirm by wear debris with plate-like shape and flake-like shape respectively.

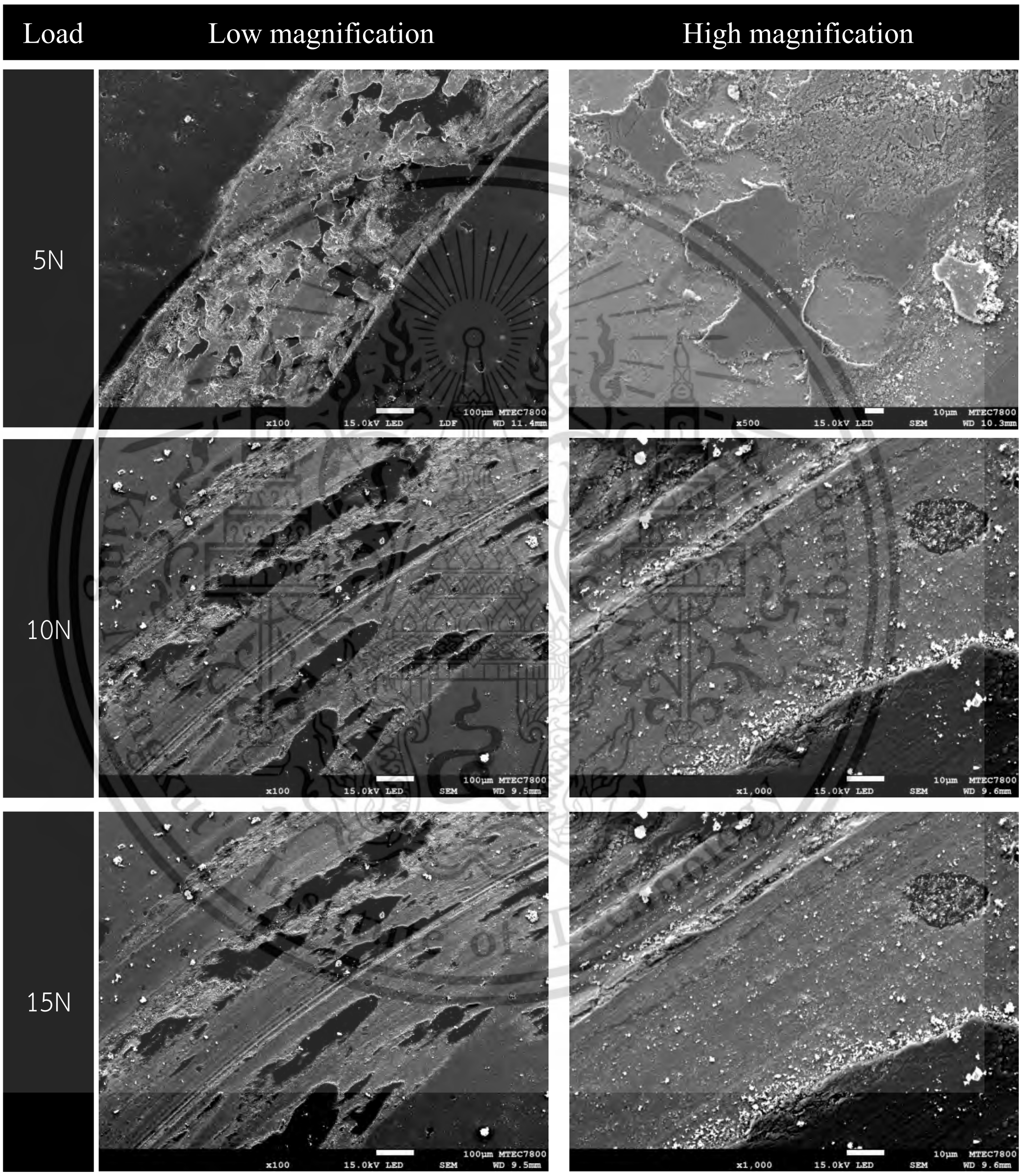

Figure 4-18 The SEM micrograph of the worn surface of sintered 10Ni composites

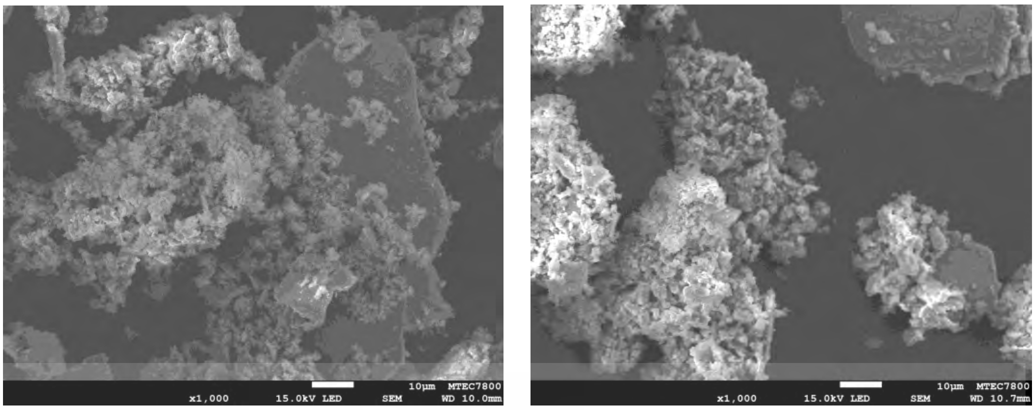

(a)Wear debris at load 5N (b) Wear debris at load 10N

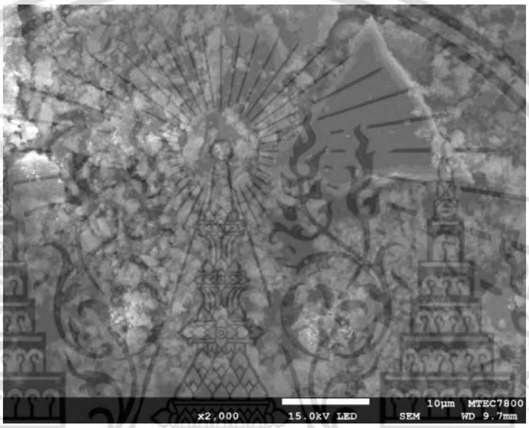

(c) Wear debris at load 15N

Figure 4-19 The SEM micrograph of wear debris of sintered 10Ni composite

4.6.5 Worn surfaces and wear debris of sintered 15Ni composite

The SEM micrographs of worn surfaces and wear debris at all normal load conditions of sintered 15Ni composite are shown in Figure 4.20 and 4.21 respectively. The mechanism of wear are abrasive wear grooves and delamination wear which confirm by wear debris with plate-like shape and flake-like shape respectively.

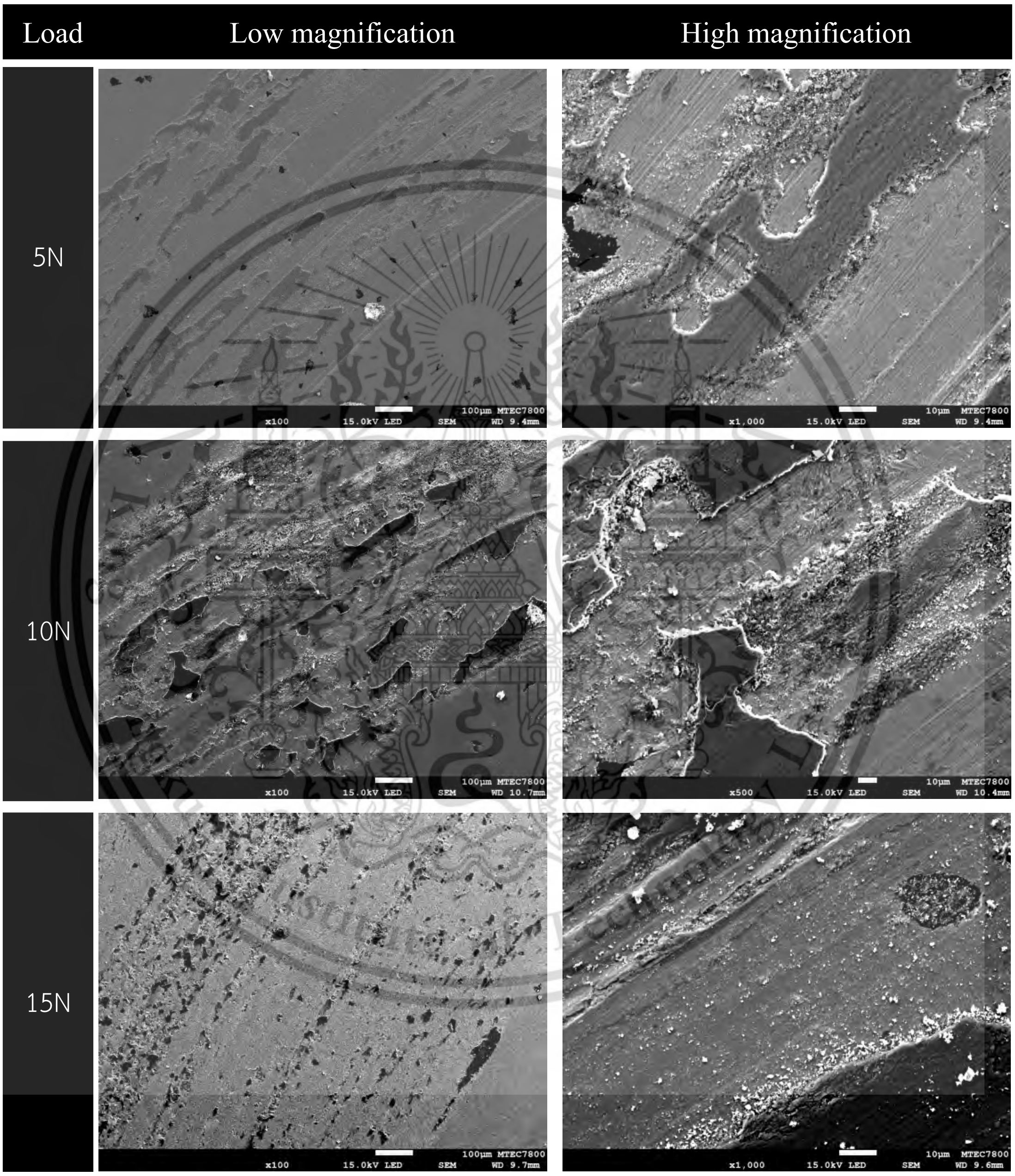

Figure 4-20 The SEM micrograph of the worn surface of sintered 15Ni composites

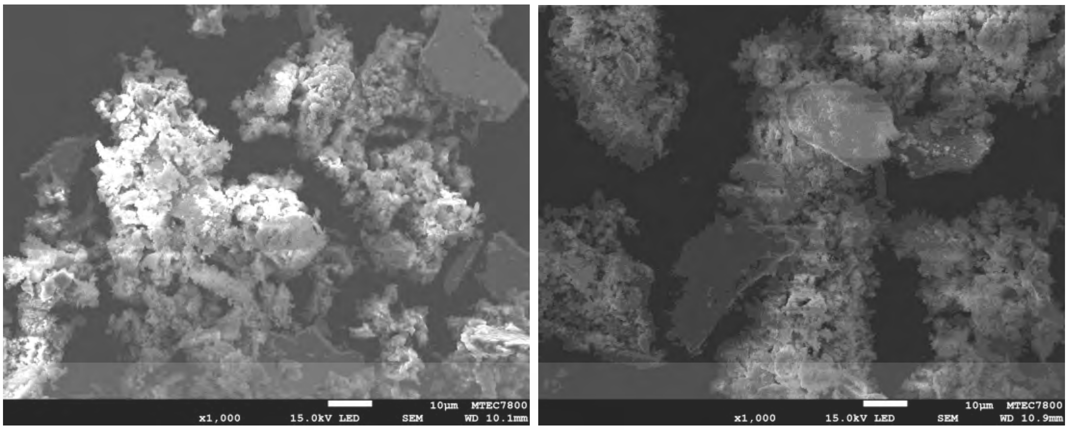

(a) Wear debris at load 5N (b)Wear debris at load10N

(c)Wear debris at load 15N

Figure 4-21 The SEM micrograph of wear debris of sintered 15Ni composite

4.6.6 Worn surfaces and wear debris of sintered 20Ni composite

The SEM micrographs of worn surfaces and wear debris at all normal load conditions of sintered 20Ni composite are shown in Figure 4.22 and 4.23 respectively. The mechanism of wear are abrasive wear grooves and delamination wear which confirm by wear debris with plate-like shape and flake-like shape respectively.

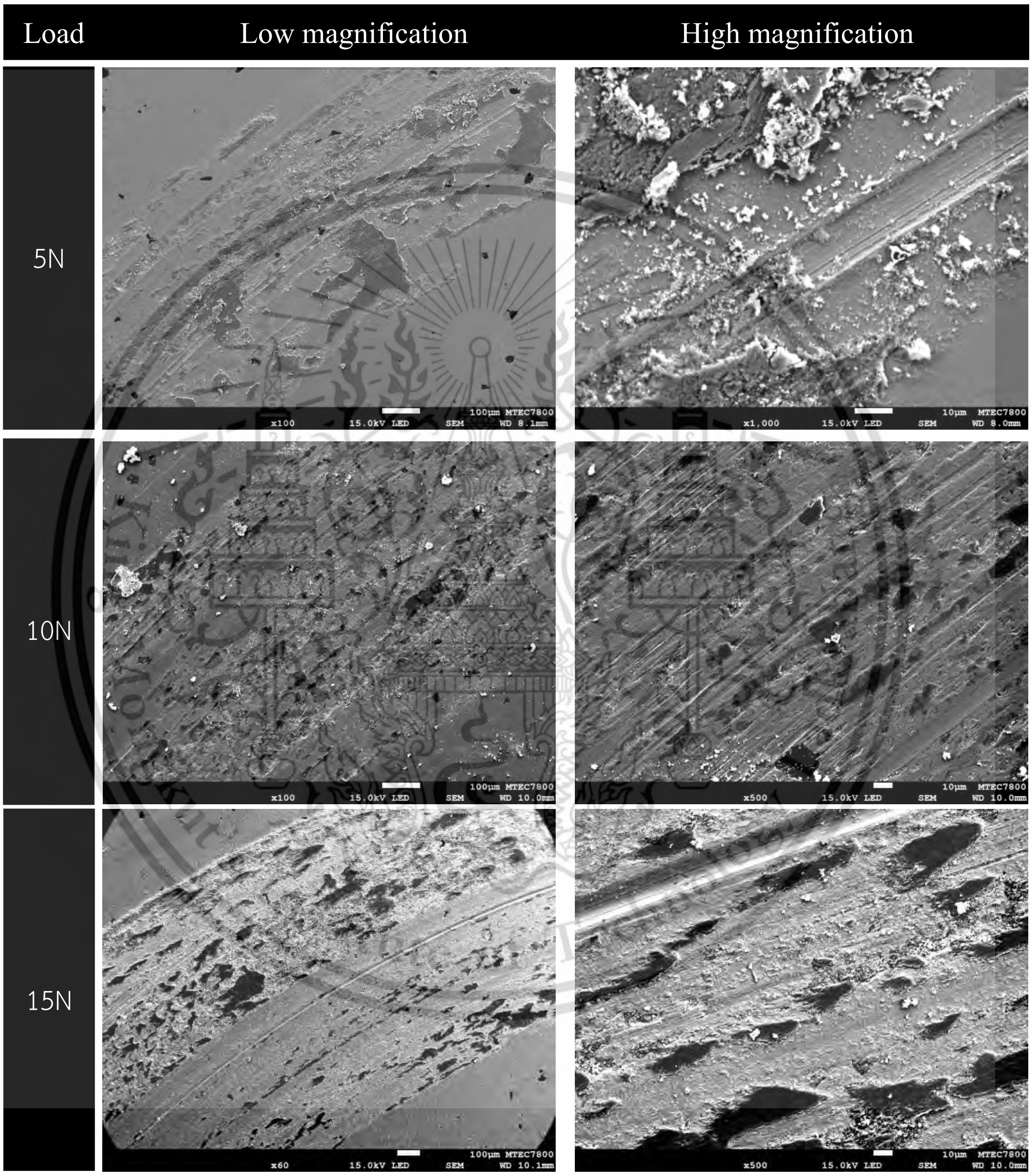

Figure 4-22 The SEM micrograph of the worn surface of sintered 20Ni composites

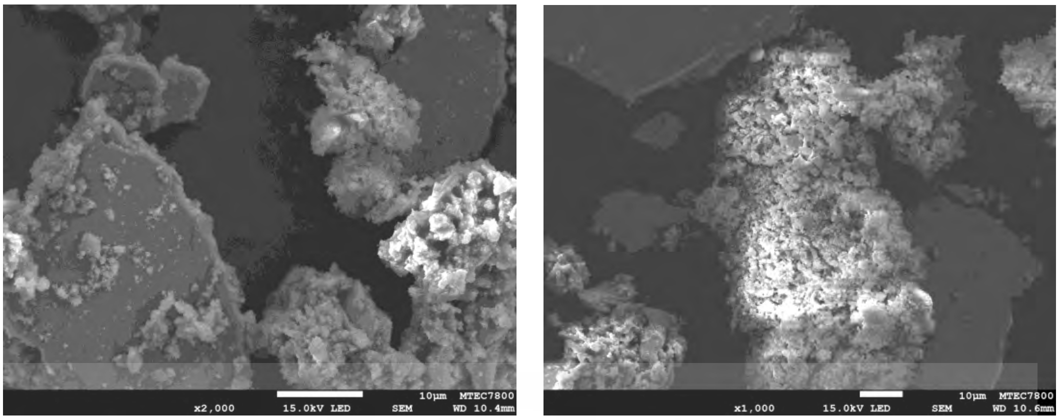

(a) Wear rate at load 5N (b) Wear rate at load 10N

(c) Wear rate at load 15N

Figure 4-23 The SEM micrograph of wear debris of sintered 20Ni composite

4.6.7 A comparative discussion of current research to other's research works

Table 4-4 shows the comparative discussion of current research to research works of other authors. In this current research, the composition of Fe-SiC and Fe-Ni-Mo-Mn-SiC from other research works is used as a foundation or reference material. From these referenced materials, Fe-1.5Mo-0.15Mn-4SiC is selected because 1.5Mo + Fe-4SiC can produce the formation of special microstructure known as ausferrite which also consists of Bainitic ferrite/Martensite-Austenite (BF/M-A). And then varied weight percentage of Ni is added to Fe-1.5Mo-0.15Mn-4SiC to promote the formation of ausferrite because Ni is known as an austenite stabilizer, and it can synergize with Mo on ausferrite formation. That is why it can be concluded that the current research aims to analyze the influence of Ni on the promotion of ausferrite.

Table 4-4 Comparison of current research to other's research works

Composition	Microstructure	Main findings
Fe-0.85Mo-4SiC Fe-1.5Mo-4SiC	Ferritic-pearlitic ductile cast iron (DCI) • Black particle • Ferrite • Pearlite • Bainite	Increase of Mo content results in lower fraction of black particle but higher fraction of ferrite, pearlite and bainite.
Fe-SiC Fe-0.5Mo-0.15Mn-4SiC Fe-0.85Mo-0.15Mn-4SiC Fe-1.5Mo-0.15Mn-4SiC	Ferritic-pearlitic ductile cast iron (DCI) • Black particle • Ferrite • Pearlite • Bainite	Molybdenum retards ferrite and pearlite transformations and promotes BF/M-A formation. It was found that a special microstructural feature called 'ausferrite' consisting of ferrite and austenite coexisted with ferrite and pearlite in sintered Fe-Mo-Si-C composites with Mo contents of ≥0.85 wt. %.

Fe-0.45Ni-0.60Mo-0.15Mn-4SiC Fe-0.90Ni-1.00Mo-0.45Cr-0.45Mn-4SiC Fe-1.80Ni-0.55Mo-0.20Mn-4SiC Fe-4.00Ni-0.50Mo-0.20Mn-4SiC	Ductile cast iron (DCI) • Black particle • Ferrite • Pearlite • Bainitic ferrite/Martensite-Austenite (BF/MA)	High Ni content could suppress ferrite and pearlite transformations and open a window for low-temperature transformations of BF/M-A and martensite.
Fe-1.5Mo-0.15Mn-4SiC Fe-0.5Ni-1.5Mo-0.15Mn-4SiC Fe-1Ni-1.5Mo-0.15Mn-4SiC Fe-1.5Ni-1.5Mo-0.15Mn-4SiC Fe-2Ni-1.5Mo-0.15Mn-4SiC	Austempered ductile iron (ADI) • Ausferrite • Bainitic ferrite/Martensite-Austenite(BF/M-A). • Black particle • Ferrite • Pearlite	High Ni content suppresses black particle counts, ferrite and pearlite transformations while increase the formation of ausferrite. It was found that Ni ≥2.0wt.% , significantly promote ausferrite formation.

CHAPTER 5

CONCLUSIONS

The present research study the influence of Nickel on microstructure, mechanical properties, and dry sliding wear behaviour of sintered Fe-Mo-Mn-Si-C-Ni composites. The major finding from experimental results summarized below.

1) All experimental sintered composites resemble austempered ductile iron with ausferrite matrix.
2) Sintered 00Ni, 05Ni, 10Ni composites with Ni content up to 1.0wt.% promote upper ausferrite formation and sintered 15Ni and 20Ni with Ni content up to 2.0wt.% promote lower ausferrite formation.
3) Sintered 10Ni composite demonstrates highest tensile strength and hardness among others. All Ni-added sintered composites displayed lower values of elongation, but 20Ni sintered composite with lower ausferrite matrix displayed the highest elongation value.
4) The increase of Nickel content results in increasing of wear rate at identical condition of normal load and sliding speed due to the influence of bainitic ferrite and austenite. However, 20Ni sintered composite has a relatively equal and lower wear rate in contrast with 00Ni.
5) The worn surface and wear debris indicate the dominant wear mechanisms are adhesive wear and delamination wear. However, there are also some abrasive, and oxidative wears in all sintered composites.

The current research laid foundational knowledge of the influence of Nickel on ausferrite promotion in Fe-Mo-Mn-SiC-(Ni) sintered composites. It was found that Nickel is a good austenite stabilizer and promote more formation of ausferrite while decrease the formation of black particles, pearlite and ferrite in sintered Fe-Mo-Mn-Si-C-(Ni) composites.

References

[1] K. S. Narasimhan, “Sintering of powder mixtures and the growth of ferrous powder metallurgy,” 2001.

[2] A. Wanalerkngam *et al.*, “Effect of carbon content on microstructure and mechanical properties of sintered Fe-Mo-Mn-C alloys,” *IOP Conf Ser Mater Sci Eng*, vol. 1137, no. 1, p. 012029, May 2021, doi: 10.1088/1757-899x/1137/1/012029.

[3] J. Lacaze, J. Sertucha, and L. Magnusson Åberg, “Microstructure of as-cast ferritic-pearlitic nodular cast irons,” *ISIJ International*, vol. 56, no. 9. Iron and Steel Institute of Japan, pp. 1606–1615, 2016. doi: 10.2355/isijinternational.ISIJINT-2016-108.

[4] K. Ruangchai, A. Wiengmoon, M. Morakotjinda, N. Tosangthum, and R. Tongsri, “Sintered Fe-Mo-Si-C alloys with ductile cast iron microstructure,” in *Journal of Physics: Conference Series*, Institute of Physics Publishing, Dec. 2018. doi: 10.1088/1742-6596/1144/1/012099.

[5] T. Nithimethakul *et al.*, “The effect of molybdenum on the microstructure and mechanical behaviour of the sintered Fe-Mo-Mn-Si-C composite,” *IOP Conf Ser Mater Sci Eng*, vol. 1137, no. 1, p. 012028, May 2021, doi: 10.1088/1757-899x/1137/1/012028.

[6] M. C. Cakir, A. Bayram, Y. Isik, and B. Salar, “The effects of austempering temperature and time onto the machinability of austempered ductile iron,” *Materials Science and Engineering: A*, vol. 407, no. 1–2, pp. 147–153, Oct. 2005, doi: 10.1016/j.msea.2005.07.005.

[7] T. Kaewkam *et al.*, “Sintered Fe-Ni-Si-C alloys,” *IOP Conf Ser Mater Sci Eng*, vol. 1137, no. 1, p. 012035, May 2021, doi: 10.1088/1757-899x/1137/1/012035.

[8] “POWDER METALLURGY TECHNOLOGY.”

[9] K. S. Narasimhan, “Sintering of powder mixtures and the growth of ferrous powder metallurgy,” 2001.

[10] T. Tsutsui, “Recent Technology of Powder Metallurgy and Applications.”

[11] S. Rao, T. Sunil, M. Sandeep, R. Kumaraswami, and A. Shravan, “A critical review on solid lubricants Effect Of Ceramic Coating On Aluminum Material To Review Mechanical And Chemical Properties View project Improvement of Machinability

of Titanium Alloys View project A CRITICAL REVIEW ON SOLID LUBRICANTS," *A Critical Review on Solid Lubricants. International Journal of Mechanical Engineering and Technology*, vol. 7, no. 5, pp. 193–199, [Online]. Available: http://www.iaeme.com/IJMET/index.asp193http://www.iaeme.com/ijmet/issues.asp?JType=IJMET&VType=7&IType=5JournalImpactFactor

[12] M. Maalekian and M. Maalekian, "Christian Doppler Laboratory for Early Stages of Precipitation The Effects of Alloying Elements on Steels (I)," 2007.

[13] X. Ding, X. Li, H. Huang, W. Matthias, S. Huang, and Q. Feng, "Effect of Mo addition on as-cast microstructures and properties of grey cast irons," *Materials Science and Engineering: A*, vol. 718, pp. 483–491, Mar. 2018, doi: 10.1016/j.msea.2018.01.095.

[14] K. M. Pedersen and N. S. Tiedje, "Graphite nodule count and size distribution in thin-walled ductile cast iron," *Mater Charact*, vol. 59, no. 8, pp. 1111–1121, Aug. 2008, doi: 10.1016/j.matchar.2007.09.001.

[15] P. A. Flinn, "Strengthening Mechanisms in Solids," *ASM, Metals Park, Ohio*, p. 17, 1962.

[16] G. Vander Voort, "Solutions for Materials Preparation, Testing and Analysis Microstructure of Ferrous Alloys." [Online]. Available: www.buehler.com

[17] M. Caruso and S. Godet, "Microstructural evolution during spheroidization annealing of eutectoid steel: Effect of interlamellar spacing and cold working," in *Advanced Materials Research*, 2010, pp. 79–84. doi: 10.4028/www.scientific.net/AMR.89-91.79.

[18] M. Ferry and W. Xu, "Microstructural and crystallographic features of ausferrite in as-cast gray iron," *Mater Charact*, vol. 53, no. 1, pp. 43–49, Sep. 2004, doi: 10.1016/j.matchar.2004.07.008.

[19] J. Lacaze, J. Sertucha, and L. Magnusson Åberg, "Microstructure of as-cast ferritic-pearlitic nodular cast irons," *ISIJ International*, vol. 56, no. 9. Iron and Steel Institute of Japan, pp. 1606–1615, 2016. doi: 10.2355/isijinternational.ISIJINT-2016-108.

[20] M. Górny, Gondek, E. Tyrała, G. Angella, and M. Kawalec, "Structure Homogeneity and Thermal Stability of Austempered Ductile Iron," *Metall Mater Trans A Phys Metall Mater Sci*, vol. 52, no. 6, pp. 2227–2237, Jun. 2021, doi: 10.1007/s11661-021-06214-8.

[21] K. Ruangchai, A. Wiengmoon, M. Morakotjinda, N. Tosangthum, and R. Tongsri, “Sintered Fe-Mo-Si-C alloys with ductile cast iron microstructure,” in *Journal of Physics: Conference Series*, Institute of Physics Publishing, Dec. 2018. doi: 10.1088/1742-6596/1144/1/012099.

[22] T. Nithimethakul *et al.*, “The effect of molybdenum on the microstructure and mechanical behaviour of the sintered Fe-Mo-Mn-Si-C composite,” *IOP Conf Ser Mater Sci Eng*, vol. 1137, no. 1, p. 012028, May 2021, doi: 10.1088/1757-899x/1137/1/012028.

[23] A. WAHI, N. MUHAMAD, A. B. SULONG, and R. N. AHMAD, “Effect of Sintering Temperature on Density, Hardness and Strength of MIM Co30Cr6Mo Biomedical Alloy,” *Journal of the Japan Society of Powder and Powder Metallurgy*, vol. 63, no. 7, pp. 434–437, 2016, doi: 10.2497/jjspm.63.434.

[24] F. B. Sweidan and H. J. Ryu, “Kinetic Monte Carlo simulations of the sintering microstructural evolution in density graded stainless steel fabricated by SPS,” *Mater Today Commun*, vol. 26, p. 101863, Mar. 2021, doi: 10.1016/j.mtcomm.2020.101863.

[25] Z. Xu, M. Hodgson, K. Chang, G. Chen, X. Yuan, and P. Cao, “Effect of Sintering Time on the Densification, Microstructure, Weight Loss and Tensile Properties of a Powder Metallurgical Fe-Mn-Si Alloy,” *Metals (Basel)*, vol. 7, no. 3, p. 81, Mar. 2017, doi: 10.3390/met7030081.

[26] C. Ornmanee *et al.*, “Effect of heating rate on sintered series 300 stainless steel,” *Songklanakarin Journal of Science and Technology*, vol. 32, May 2010.

[27] A. P. G. Chaves, D. M. A. Centeno, M. Masoumi, and H. Goldenstein, “Effect of the Microstructure on the Wear Resistance of a Pearlitic Steel,” *Materials Research*, vol. 23, no. 2, 2020, doi: 10.1590/1980-5373-mr-2019-0605.

[28] M. Krbata, M. Eckert, J. Majerik, and I. Barenyi, “Wear Behaviour of High Strength Tool Steel 90MnCrV8 in Contact with Si3N4,” *Metals (Basel)*, vol. 10, no. 6, p. 756, Jun. 2020, doi: 10.3390/met10060756.

[29] E. Rabinowicz, L. A. Dunn, and P. G. Russell, “A study of abrasive wear under three-body conditions,” *Wear*, vol. 4, no. 5, pp. 345–355, Sep. 1961, doi: 10.1016/0043-1648(61)90002-3.

[30] W. Yi-Ling and W. Zi-Shan, “An analysis of the influence of plastic indentation on three-body abrasive wear of metals,” *Wear*, vol. 122, no. 2, pp. 123–133, Mar. 1988, doi: 10.1016/0043-1648(88)90073-7.

[31] C. Spero, D. J. Hargreaves, R. K. Kirkcaldie, and H. J. Flitt, “Review of test methods for abrasive wear in ore grinding,” *Wear*, vol. 146, no. 2, pp. 389–408, Jun. 1991, doi: 10.1016/0043-1648(91)90077-8.

[32] A. G. Wang and I. M. Hutchings, “The number of particle contacts in two-body abrasive wear of metals by coated abrasive papers,” *Wear*, vol. 129, no. 1, pp. 23–35, Jan. 1989, doi: 10.1016/0043-1648(89)90276-7.

[33] A. Misra and I. Finnie, “A classification of three-body abrasive wear and design of a new tester,” *Wear*, vol. 60, no. 1, pp. 111–121, Apr. 1980, doi: 10.1016/0043-1648(80)90252-5.

[34] K. Endo and H. Goto, “Effects of environment on fretting fatigue,” *Wear*, vol. 48, no. 2, pp. 347–367, Jun. 1978, doi: 10.1016/0043-1648(78)90232-6.

[35] A. W. Batchelor, G. W. Stachowiak, and A. Cameron, “The relationship between oxide films and the wear of steels,” *Wear*, vol. 113, no. 2, pp. 203–223, Dec. 1986, doi: 10.1016/0043-1648(86)90121-3.

[36] A. Dréano, S. Fouvry, and G. Guillonneau, “A tribo-oxidation abrasive wear model to quantify the wear rate of a cobalt-based alloy subjected to fretting in low-to-medium temperature conditions,” *Tribol Int*, vol. 125, pp. 128–140, Sep. 2018, doi: 10.1016/j.triboint.2018.04.032.

[37] P. Saal *et al.*, “In Situ Study of the Influence of Nickel on the Phase Transformation Kinetics in Austempered Ductile Iron,” *Metall Mater Trans A Phys Metall Mater Sci*, vol. 47, no. 2, pp. 661–671, Feb. 2016, doi: 10.1007/s11661-015-3261-1.

[38] O. Gumienny, “Carbidic bainitic and ausferritic ductile cast iron,” *Archives of Metallurgy and Materials*, vol. 58, no. 4, pp. 1053–1058, 2013, doi: 10.2478/amm-2013-0125.

[39] N. I. Araya, C. Binder, A. N. Klein, G. Hammes, J. D. B. De Mello, and C. Aguilar, “Effect of heat treatments and SiC content in the mechanical properties and microstructure of self-lubricating steels,” *Materials Research*, vol. 21, no. 1, 2018, doi: 10.1590/1980-5373-mr-2017-0664.

[40] J. D. B. De Mello, C. Binder, G. Hammes, R. Binder, and A. N. Klein, “Tribological behaviour of sintered iron based self-lubricating composites,” *Friction*, vol. 5, no. 3. Tsinghua University Press, pp. 285–307, Sep. 01, 2017. doi: 10.1007/s40544-017-0186-2.

[41] M. C. Cakir, A. Bayram, Y. Isik, and B. Salar, “The effects of austempering temperature and time onto the machinability of austempered ductile iron,” *Materials Science and Engineering: A*, vol. 407, no. 1–2, pp. 147–153, Oct. 2005, doi: 10.1016/j.msea.2005.07.005.

[42] H. Zhou *et al.*, “Microstructure and mechanical behaviors of grinding balls produced by dual matrix structure two-step austempering process,” *Journal of Materials Research and Technology*, vol. 9, no. 3, pp. 4672–4681, 2020, doi: 10.1016/j.jmrt.2020.02.095.

[43] M. Górny, Gondek, E. Tyrała, G. Angella, and M. Kawalec, “Structure Homogeneity and Thermal Stability of Austempered Ductile Iron,” *Metall Mater Trans A Phys Metall Mater Sci*, vol. 52, no. 6, pp. 2227–2237, Jun. 2021, doi: 10.1007/s11661-021-06214-8.

[44] C. Binder, T. Bendo, R. V. Pereira, G. Hammes, J. D. B. de Mello, and A. N. Klein, “Influence of the SiC content and sintering temperature on the microstructure, mechanical properties and friction behaviour of sintered self-lubricating composites,” *Powder Metallurgy*, vol. 59, no. 5, pp. 384–393, Oct. 2016, doi: 10.1080/00325899.2016.1250036.

[45] N. Araya *et al.*, “Study of silicon carbide dissociation into Fe and Fe C matrixes produced by die pressing and sintering,” *Mater Chem Phys*, vol. 253, Oct. 2020, doi: 10.1016/j.matchemphys.2020.123442.

[46] M. Morakotjinda, T. Yotkaew, B. Vetayanugul, A. Wanalerkngam, and R. Tongsri, “Promotion of ausferrite formation in as-sintered Fe–Mo–Si–C-(Cu) composites due to Cu addition,” *Mater Chem Phys*, vol. 296, Feb. 2023, doi: 10.1016/j.matchemphys.2022.127226.

[47] S. Daber and P. Prasad Rao, “Formation of strain-induced martensite in austempered ductile iron,” *J Mater Sci*, vol. 43, no. 1, pp. 357–367, Jan. 2008, doi: 10.1007/s10853-007-2258-6.

[48] K. Ruangchai *et al.*, “Microstructure, hardness and wear properties of sintered Fe-Mo-Si-C steels with spheroidal graphite iron/compacted graphite iron-like,”

in *Key Engineering Materials*, Trans Tech Publications Ltd, 2017, pp. 47–52. doi: 10.4028/www.scientific.net/KEM.751.47.

[49] E. Colin-García, A. Cruz-Ramírez, G. Reyes-Castellanos, J. A. Romero-Serrano, R. G. Sánchez-Alvarado, and M. Hernández-Chávez, “Influence of nickel addition and casting modulus on the properties of hypo-eutectic ductile cast iron.”

[50] J. Lacaze, P. Larranaga, I. Asenjo, R. Suárez, and J. Sertucha, “Influence of 1 wt-% addition of Ni on structural and mechanical properties of ferritic ductile irons,” *Materials Science and Technology*, vol. 28, no. 5, pp. 603–608, 2012, doi: 10.1179/1743284711Y.0000000100.

[51] E. Akbarzadeh Chiniforush, N. Iranipour, and S. Yazdani, “Effect of nodule count and austempering heat treatment on segregation behavior of alloying elements in ductile cast iron,” *China Foundry*, vol. 13, no. 3, pp. 217–222, May 2016, doi: 10.1007/s41230-016-6034-6.

[52] B. Wang *et al.*, “Study of Ausferrite Transformation Kinetics for Austempered Ductile Irons with and without Ni,” in *SAE Technical Papers*, SAE International, 2016. doi: 10.4271/2016-01-0421.

[53] N. Elmasry and A. Mahdy, “Influence of austempering temperature on microstructure and properties of ductile irons,” 2013. [Online]. Available: https://www.researchgate.net/publication/282326627

[54] J. Wang, Y. Cheng, Y. Zhang, Z. Yin, X. Hu, and Q. Yuan, “Friction and wear behavior of microwave sintered Al2O3/TiC/GPLs ceramic sliding against bearing steel and their cutting performance in dry turning of hardened steel,” *Ceram Int*, vol. 43, no. 17, pp. 14827–14835, Dec. 2017, doi: 10.1016/j.ceramint.2017.07.231.

[55] D. Muhammad Nuruzzaman and M. Asaduzzaman Chowdhury, “Effect of Load and Sliding Velocity on Friction Coefficient of Aluminum Sliding Against Different Pin Materials,” *American Journal of Materials Science*, vol. 2, no. 1, pp. 26–31, Feb. 2012, doi: 10.5923/j.materials.20120201.05.

[56] J. F. Archard, “Contact and rubbing of flat surfaces,” *J Appl Phys*, vol. 24, no. 8, pp. 981–988, 1953, doi: 10.1063/1.1721448.

[57] R. L. Deuis, ; C Subramanian, and J. M. Yellupb, “DRY SLIDING WEAR OF ALUMINIUM COMPOSITES-A REVIEW,” 1997.

[58] E. Zdravecká, J. Tkáčová, and M. Ondáč, “Effect of microstructure factors on abrasion resistance of high-strength steels,” *Research in Agricultural Engineering*, vol. 60, no. 3, pp. 115–120, 2014, doi: 10.17221/20/2013-rae.

APPENDIX A:

CONFERENCE PARTICIPATION

The 12th TSME International Conference on Mechanical Engineering
13th – 16th December 2022
Phuket, Thailand

AMM0003

The Effect of Nickel on The Microstructure and Mechanical Behaviour of The Sintered Fe-Mo-Mn-Si-C Composite

Zayar Min Htike[1], Jittraporn Wongsa-Ngam[1], Naoto Ohtake[2], Monnapas Morakotjinda[3], Thanyaporn Yotkaew[3], Ruangdaj Tongsri[3,*]

[1]Department of Mechanical Engineering, School of Engineering, King Mongkut's Institute of Technology of Ladkrabang (KMITL), Bangkok 10520, Thailand
[2]Department of Mechanical Engineering, School of Engineering, Tokyo Institute of Technology, Tokyo 152-8550, Japan
[3]Particulate Materials Processing Technology (PMPT), Metal and Manufacturing Process Research Group, National Metal and Materials Technology Center, 114 Paholyothin Road, Khlong Nueng, Klong Luang, Pathum Thani 12120, Thailand

* Corresponding author E-mail: ruangdt@mtec.or.th

AUTHOR BIOGRAPHY

Author:	Mr. Zayar Min Htike
Nationality:	Myanmar
Email:	64601185@kmitl.ac.th

Education:

2023	Master of Automotive and Advance Transportation Engineering Faculty of Engineering, King Mongkut's Institute of Technology Ladkrabang
2019	Bachelor of Engineering, Mechanical Engineering Mandalay Technological University (COE)

Conference Participation Publications:

[1] Zayar Min Htike, Jittraporn Wongsa-Ngam, Naoto Ohtake, Monnapas Morakotjinda, Thanyaporn Yotkaew, Ruangdaj Tongsri "The Effect of Nickel on The Microstructure and Mechanical Behaviour of The Sintered Fe-Mo-Mn-Si-C Composite", 12th TSME International Conference on Mechanical Engineering Proceedings, 2022.